Multi-Sensor Blue LED and Touch Probe Inspection System

MULTI-SENSOR BLUE LED AND TOUCH PROBE INSPECTION SYSTEM

By

KAI XUE, B.ENG.

A Thesis

Submitted to the School of Graduate Studies

in Partial Fulfilment of the Requirements

for the Degree

Master of Applied Science

McMaster University

MASTER OF APPLIED SCIENCE (2015) McMaster University

(Mechanical Engineering) Hamilton, Ontario, Canada

TITLE: Multi-Sensor Blue LED and Touch Probe Inspection System

AUTHOR: Kai Xue,

B.Eng., Mechanical Eng. and Automation,

Nanjing University of Aeronautics and Astronautics, China

SUPERVISOR: Dr. Allan D. Spence

NUMBER OF PAGES: xvii, 105

Abstract

In dimensional metrology, contact and non-contact measurement methods each have their own respective strengths and weaknesses. Touch-trigger probes have low uncertainty, and perform well inside deep holes, but have a relatively slow data acquisition speed. By contrast, non-contact digitizers collect high density surface point clouds in seconds, and are much less likely to suffer from sensor collision with the part, but have a higher uncertainty than touch probes. In sheet metal forming, iterative design of the stamping die is needed due to the springback of the sheet metal part. Holes or other features of first article parts may be significantly out of tolerance, so the tactile measurement path created from the Computer Aided Design (CAD) nominal has to be adjusted to avoid cosine error. In more serious cases, probe collisions or missed touches may occur. When measuring holes in thin sheet metal, determination of the touch probe path height is also a challenge if the actual surface location differs from the nominal.

To solve this problem and seize the complimentary advantages of contact and non-contact measurement methods, a multi-sensor blue Light Emitting Diode (LED) snapshot sensor and touch-trigger probe inspection system was developed, and affixed to a Coordinate Measuring Machine (CMM). The tactile measurement path was adjusted according to the approximate positions and sizes of the features obtained from the scanner data. The system includes an in-house designed calibration target for scanner calibration and a lightweight 2-axis rotary table for multiple-orientation scanning as well. Software in programming language C for interacting with the scanner and the CMM was developed. A sample stamped sheet metal automobile part was experimentally measured. This system is currently applied to an orthogonal CMM. Suggested future works include implementation on non-Cartesian CMMs, such as articulated arm CMMs, or Computer Numerical Control (CNC) machine tools.

Acknowledgements

I would like to express my sincerest gratitude to my supervisor Dr. Allan D. Spence for his patience, valuable guidance, understanding, and continuous encouragement during this thesis work. I appreciate that he has provided me an excellent atmosphere for doing research, and arranged financial support through NSERC. I would like to thank him very much for offering me opportunities to attend both academic and industrial conferences where I learned about cutting-edge research and met excellent researchers in related fields. He is so considerate and thoughtful that sometimes he is more like a family than a supervisor.

Very special thanks to my colleague Venu Kurella who has offered me valuable advice, insights, and encouragement throughout my thesis work. I must also acknowledge the Mechanical Engineering technicians, Michael Lee, Mark MacKenzie, Ron Lodewyks, and John Colenbrander for their kind support in machining. Special appreciation goes to Michael for his patient guidance in machining, and to Mark for welding workpieces for me. Thank Terry Wagg for waterjet cutting workpieces for me. Also, thank Diaa Elkott and Tarek Hamdan for the help with analog probe measurement.

Finally, I would like to thank my parents for their love, support and guidance through my studies and throughout life. The love they provide me is endless and incomparable.

Table of Contents

List of Tables

List of Figures

Nomenclature

CAD	Computer Aided Design
LED	Light Emitting Diode
CMM	Coordinate Measuring Machine
CNC	Computer Numerical Control
DMIS	Dimensional Measuring Interface Standard
LCS	Local Coordinate System
GCS	Global Coordinate System
MCS	Machine Coordinate System
PCS	Part Coordinate System
HTM	Homogeneous Transformation Matrix
OLS	Orthogonal Least Squares
FEA	Finite Element Analysis
ICP	Iterative Closest Point
CTE	Coefficient of Thermal Expansion
RMS	Root Mean Square
RSS	Root Sum of Squares

Chapter 1

Introduction

1.1 Motivation for This Work

Dimensional metrology plays an important role in quality management and process control [1]. Productive metrology not only facilities new product design, verifies product quality, but also gains necessary process parameters for optimizing the following production processes [2]. With new developments in production, the requirements for innovative metrology methods and techniques become increasingly diverse. Contact and non-contact measurement methods each have their own respective strengths and weaknesses [3],[4]. Touch-trigger probes can achieve low uncertainty [5], and perform well for surfaces that are inaccessible to non-contact scanners, such as deep holes. However, they have a relatively slow data acquisition speed of approximately 2 points per second. Moreover, soft material surfaces may deform when touched, or even be permanently damaged. By contrast, non-contact digitizers collect high density surface point clouds in seconds, and are much less likely to suffer from sensor collisions with the part. However, they have higher uncertainty than touch probes, and are constrained by visibility and specular reflection difficulties.

Dimensional metrology is in large demand in automotive industry, where car panels are produced in sheet metal forming processes with stamping or punch tools. In metal forming, the designed shape of the workpiece may not be obtained because of springback [6],[7],[8]. Therefore, design iteration is required. During first article tryout and inspection, significant adjustment of stamping or punch die is common. These adjustments are needed until repeatable and correct surface shape and hole features are achieved. Parts manufactured at early production stage may deviate significantly from nominal. Consequently, when touch probing the sheet metal part, Dimensional Measuring Interface Standard (DMIS) inspection program created using the CAD nominal geometry can no longer be used without introducing significant part surface cosine error. In more extreme cases, touch probes may miss touches or collide with the part.

In thin sheet metal measurement, a second problem arises when touch probing holes. If the surface location differs from the nominal, the spherical probe cannot correctly contact the hole side. A cylindrical probe could be used, but only in the case where probe shaft is exactly normal to the sheet. Currently, this problem is solved in a time consuming manner by taking sample points on the surrounding sheet surface to ascertain the actual surface location. Hole measurement points are then collected by adjusting the probe path to be half of the nominal sheet thickness below the surface.

For inspection of sculptured surfaces or holes and other features on them, multiple-orientation scanning is required for full part surface coverage [9]. In this case, sensor or part tilt/rotate axis is needed in addition to the CMM linear X, Y, and Z axes. Determination of whether the tilt/rotate axis should be added to the sensor or the part is based on the weight of the sensor, the carrying capability of the CMM component, the type of machine that the sensor is affixed to, and so forth. Coordinate system registration is needed for transforming point clouds obtained from different orientations by the sensor into a common coordinate system.

1.2 Thesis Objectives

The objective of this thesis is to develop a multi-sensor inspection system consisting of a blue LED structured light scanner and a touch-trigger probe mounted on a CMM. The system takes advantage of the best characteristics of contact and non-contact sensors, and is able to solve the described problems in tactile measurement of thin sheet metal part. Additionally, a tilt/rotate 2-axis rotary table needs to be designed and constructed for multiple-orientation scanning of the workpiece, which results in a 5-axis CMM.

1.3 Contributions of This Thesis

The significant contributions provided by this thesis include:

1. Developed a multi-sensor inspection system for successful tactile measurement of thin sheet metal, and other manufactured parts.
2. The developed inspection system is ready to be migrated to portable CMMs, CNC machines, and robots.

3. Mechanically aligned the scanner with the CMM using calibration target for extrinsic calibration of the scanner.
4. Developed software for interacting simultaneously with the scanner and the CMM, such as outputting point clouds, and feature size and position measured by the scanner, recording the CMM coordinates, and so forth.
5. Designed and constructed a lightweight 2-axis rotary table for multiple-orientation scanning to cover the whole part.
6. Developed program for transforming point cloud data obtained from different orientations by the scanner into a common coordinate system, namely coordinate system registration.

1.4 Scope of Thesis

The remainder of the thesis is organized as follows:

Chapter 2 is literature review, in which dimensional metrology sensors, including contact touch probes and non-contact scanners, are demonstrated. Existing problems in the sheet metal tactile measurement are then described. The solution using multi-sensor inspection system is proposed. Multi-sensor systems that have been developed by other researchers for different purposes are reviewed. Following that, extrinsic calibration of the scanner, multiple-orientation scanning, and coordinate system registration are described. Finally, a method for acquiring the squareness errors of the CMM is implemented.

Chapter 3 describes the overall architecture of the inspection system. The employed hardware and software, their properties, and the connection between them are presented.

In Chapter 4, mechanical minimization of the angular misalignment between the scanner and the CMM axes is shown. The processes of touch probing and scanning the calibration target are described.

Chapter 5 presents the detailed workflow of the multi-sensor synergistic inspection. The workflow includes creation of the nominal touch probe inspection program, scanner measurement of the workpiece, and adjustment of the touch probe measurement path. Transformation of the data between different coordinate systems is shown. Compensation of the counter card reading for the linear displacement errors and squareness errors of the CMM is also described.

The design process of the lightweight 2-axis rotary table is provided in Chapter 6. The dimension design of the table components, Finite Element Analysis (FEA), and strength check of the key components are all presented in this chapter.

Chapter 7 demonstrates multiple-orientation scanning of the part. Digitization, coordinate system registration, merging, and processing of the point clouds are described here, followed by 3D comparison of the acquired point cloud with CAD model. Finally, measurement with analog touch probe for verification is presented, and the collected data are compared with the scanner data.

Chapter 8 confirms the high efficiency and accuracy of the developed multi-sensor inspection system with experiments on a stamped automotive sheet metal part.

Multiple-orientation scanning of the part was also carried out with the designed rotary table. Measurement results are presented and analyzed. Measurement uncertainty of the multi-sensor system was investigated.

Chapter 9 concludes this thesis work, and suggests future work.

Chapter 2

Literature Review

2.1 Dimensional Metrology

The life cycle of a product involves a series of activities, ranging from product planning and development to production and sales (Fig. 2.1). Metrology should be implemented in any phase of the life cycle; otherwise the costs for fixing the errors increase by a factor of ten for every further phase [2]. The involved measurement activities are: (1) New product-oriented measurements for model verification. (2) Test of conformity to specifications. (3) Measurements for manufacturing process control. (4) Equipment qualification, e.g. machine tool verification. Metrology in the manufacturing process is of great importance in the value chain. It not only verifies whether the part features conform to the engineering specifications, but also gains process parameter values for optimizing the following manufacturing processes. Moreover, manufacturing metrology also helps the development of the next product version or design review. Measurement methods fall into two categories: contact and non-contact measurements.

2.1.1 Touch Probing System

There are two touch probing systems. One is touch-trigger probing system that measures discrete points at the speed of approximately 2 points per second and has to retract from the workpiece following detection of contact with the workpiece. The other is scanning probing system in which the probing element keeps in contact with the workpiece and hundreds of points are digitized per unit time. Consequently, touch-trigger probing system is mostly used in the measurement of standard geometric features, while scanning probing system is more appropriate for sculptured surfaces and inspection of form deviation [10]. Touch probes, even scanning probes, have a relatively slow digitizing speed compared with non-contact digitizers and are crash-prone, but have lower uncertainty (within micrometers) and can measure surfaces that are inaccessible to non-contact scanners, such as deep holes.

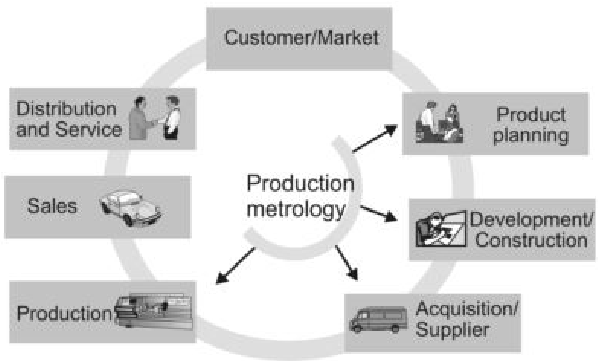

Fig. 2.1: The role of metrology in a product life cycle [2].

2.1.1.1 Touch-Tigger Probing System

Touch-trigger probes only report two states of the system, contact or no contact. The main working principle of touch-trigger probes exists in an electric circuit [3]. The circuit switch is open when there is contact between the stylus and the workpiece, otherwise it is closed. The resistance of the circuit is measured. When it exceeds a threshold value, the trigger signal is generated (Fig. 2.2(a)).

The touch-trigger probe used for this thesis is Renishaw® TP6 (Fig. 2.2(b)). It is called a kinematic resistive probe. It consists of a pivotal plate, three pairs of bearing points, and a helical compression spring. Each of the three cylindrical pegs sits on two separated electric contacts, which in total constrain the six degrees of freedom of the stylus. When the stylus contacts the workpiece, it is deflected by the probing force, which reduces one of the six constraints, and thus increasing the resistance of the circuit [3].

There are also other touch-trigger probing systems using piezo sensors for detection of contact.

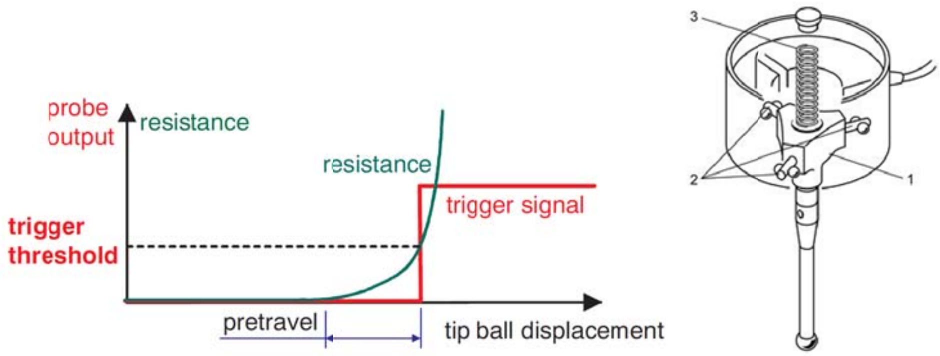

Fig. 2.2: Working principle of touch-trigger probing system: (a) Response characteristic [3], (b) Renishaw® TP6 probe [11] (1. Pivotal plate, 2. Bearing points, 3. Compression spring).

The position vector of tip ball center, $\mathbf{r}_p$, in the probe coordinate system and the effective tip ball correction vector **b** (Fig. 2.3) need to be determined for correct measurement results. They are influenced by elastic deformations of stylus stem, tip ball, and workpiece caused by probing force, as well as the pretravel variation of the probing system (pretravel is the stylus displacement upon contact with the workpiece before contact detection) [10]. Therefore, probing system qualification needs to be performed to obtain effective tip ball diameter that takes these effects into account (Fig. 2.4). A spherical artifact is usually used for 3D spherical tip qualification. It is preferred because it has normal vectors in any spatial direction, and can be positioned regardless of orientation. The effective tip ball diameter can be calculated from the measured spherical artifact diameter $d_a^{'}$ with probe compensation off, and the actual spherical artifact diameter d_a provided by the manufacturer:

$$d_{eff} = d_a^{'} - d_a \tag{2.1}$$

To ensure minimal non-repeatability errors, similar conditions have to be maintained during qualification and measurement. This will lead to consistency in probing force direction and operating mode.

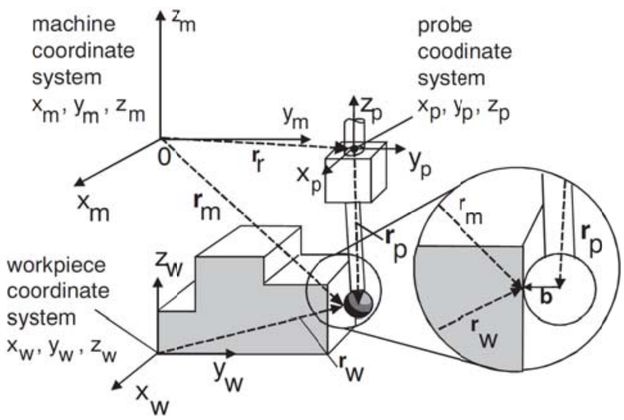

Fig. 2.3: Coordinate systems of touch probing measurement [3].

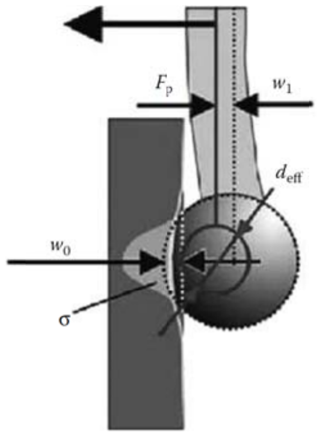

Fig. 2.4: Effective tip ball diameter [10]. (F_p : Probing force; w_0 : Elastic deformation of tip ball and workpiece; w_1 : Elastic deformation of stylus stem; σ : Hertzian contact stress.)

2.1.1.2 Scanning Probing System

In contrast with touch-trigger probing systems, a scanning probing system can measure the probing normal vector. A transducer is embedded in the system for measuring the displacement of the tip ball, s, so that the position vector $\mathbf{r}_p$ of tip ball center in the probing coordinate system $x_p y_p z_p$ can be determined (Fig. 2.3). Most common principles of the length measurement transducer are inductive, capacitive, resistive, optical, and scale-based systems. A Zeiss Prismo CMM [12] was used in this thesis. It is equipped with an inductive length measuring system (Fig. 2.5). As the magnetically soft metal core moves inside of the coil, the inductance L changes with its length inside the coil. Linear responses of the transducer are preferred because of their constant sensitivity in the measurement range. However, the function $L = f(s)$ is hyperbolic. To obtain a more linear response, a differential setup with two coils is usually used [3].

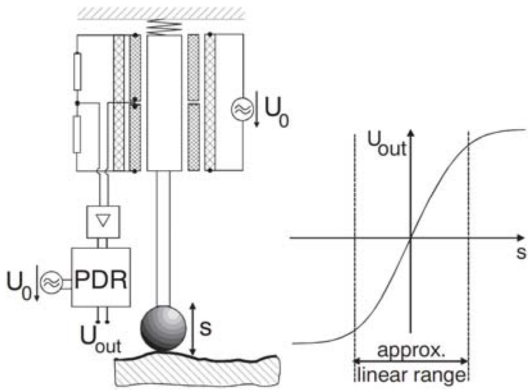

Fig. 2.5: Working principle of scanning probing system (inductive transducer) [3].

2.1.1.3 Cosine Error

A commonly seen error in measurement with touch probing systems is cosine error. After qualification, the effective tip ball diameter is recorded. During measurement, the CMM tracks the center of the tip ball upon contact with the workpiece. If probe compensation is on, the effective tip ball diameter is added (e.g. hole) or subtracted (e.g.

stud) in the direction in which the probe is moving (Fig. 2.6(a)). Consequently, the cosine error occurs when the probe is moving in a non-normal direction to the measured surface [13] (Fig. 2.6(b)). This problem happens when the feature of a manufactured workpiece deviates from the designed nominal geometry.

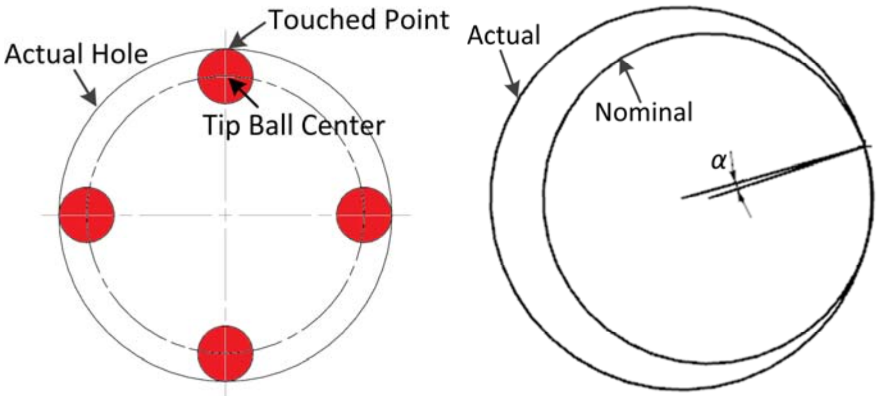

Fig. 2.6: Illustration of cosine error: (a) Probe compensation, (b) Cosine error.

2.1.2 Non-Contact Blue LED Structured Light Scanner

Optical 3D measurement techniques are widely used in industry especially for sculptured surfaces because optical sensors are capable of high density data acquisition, high speed digitizing, and have no contact with the workpiece during measurement. However, they have higher uncertainty, and geometric constraints such as visibility and pixel resolution. Moreover, they suffer from specularity difficulties and ambient light influence [14]. Their applications include, but are not limited to, control for intelligent robots, obstacle detection for vehicle guidance, dimensional inspection of stamping panels, and inline metrology for mass production of car bodies. Digitizing techniques range from time of flight, Moiré, interferometry, photogrammetry, to laser tracking system, laser scanning, and structured light [15].

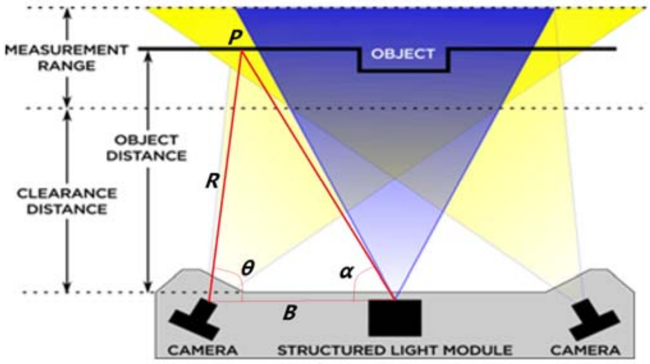

Fig. 2.7: Working principle of LMI® Gocator 3110 blue LED scanner [16].

The optical sensor used for this thesis was LMI® Gocator 3110 [17] (Fig. 2.7). It is a structured light scanner integrating Structured Light Modulator, a blue LED, and two cameras into one single device. The blue light scanning has better performance than white light scanning because it has a longer lasting light source, is less affected by temperature due to the utilization of LEDs, and can filter out the ambient light even in a well-lit room [18]. The structured light method is categorized as active triangulation. Either independent triangulation or stereo correlation mode can be selected when operating the blue LED sensor. In independent triangulation mode, each camera independently forms the triangulation geometry with the surface point and the structured light projector, using the intrinsic parameters calibrated when the sensor was manufactured. As shown in Fig. 2.7, their relationship can be expressed as [19]:

$$R = B\frac{\sin\alpha}{\sin(\alpha+\theta)} \tag{2.2}$$

In this mode, the target point only needs to be visible to one of the cameras. By contrast, in stereo correlation mode, the object surface point is captured by both of the two cameras. The two cameras and the surface point form the triangulation geometry. When measuring simple-shaped objects, more stable measurement result can be obtained in stereo correlation mode. However, independent triangulation mode performs better on objects with sculptured surfaces or protruding features that may cause occlusion [16].

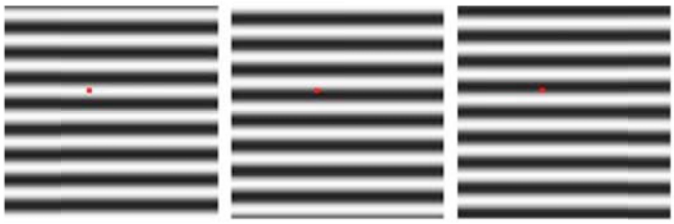

Fig. 2.8: Structured light patterns for phase-shifting algorithm [20].

There are various 3D surface imaging techniques of structured light. The one implemented in the blue LED sensor is phase shift. In the phase-shifting algorithm, a sequence of sinusoidal patterns is projected onto the object (Fig. 2.8). The patterns modulated by the object surfaces are captured by the two cameras. The intensities for each pixel of the three captured images can be expressed as [21]:

$$\begin{aligned} I_1(x,y) &= I'(x,y) + I''(x,y)\cos(\phi(x,y) - \theta) \\ I_2(x,y) &= I'(x,y) + I''(x,y)\cos(\phi(x,y)) \\ I_3(x,y) &= I'(x,y) + I''(x,y)\cos(\phi(x,y) + \theta) \end{aligned} \tag{2.3}$$

where $I'(x,y)$ is the average intensity, $I''(x,y)$ the intensity modulation amplitude, and θ the constant phase shifting angle. The modulo 2π phase $\phi(x,y) \in (0, 2\pi]$ can be derived from Eqn. (2.3):

$$\phi(x,y) = \arctan\left(\sqrt{3}\frac{I_1 - I_3}{2I_2 - I_1 - I_3}\right) \tag{2.4}$$

Following that, multiples of 2π are added to or subtracted from $\phi(x,y)$ to fix the phase discontinuities caused by multiple fringes in the fringe patterns and obtain a continuous phase map. This process is called phase unwrapping (Fig. 2.9). Finally, a calibration process is needed to convert the unwrapped phase and obtain the depth information of the object [20].

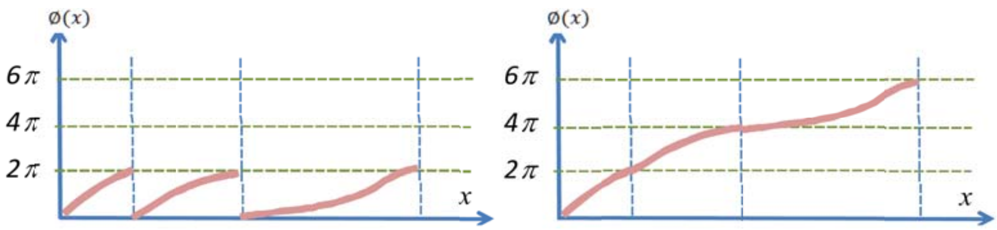

Fig. 2.9: Phase unwrapping process [19]: (a) Wrapped and (b) Unwrapped phase map.

Data collected in the Local Coordinate System (LCS) of the scanner needs to be transformed to a Global Coordinate System (GCS) by combining with the CMM X, Y and Z coordinates. When mounted on a CMM, the structured light scanner is more convenient to use than a laser line scanner as it can capture an entire 3D surface in view when standing still. There is no need for error-prone real-time synchronization with the CMM axis positions. Built-in measurement tools for 3D feature recognition are offered all inside the sensor.

2.2 Problem in Sheet Metal Measurement

The stress-strain curve for a common type of metal is shown in Fig. 2.10. When the loading stress is larger than the yield strength of the material, elastic-plastic straining occurs. When the stress is unloaded, the elastic deformation vanishes, this process is called springback. In sheet metal forming process, the springback of the formed part upon unloading the punch or the blankholder is commonly seen [6],[7]. Consequently, the desired shape of the workpiece cannot be obtained if the tools are created according to the design. Therefore, design iteration of stamping or punch die is needed in the product design process until the required surface shape or position and size of hole, slot, and other features are achieved [22],[23]. During transition from design to manufacture, the produced sheet metal may deviate very much from nominal, which is also commonly seen in other product designs. This leads to difficulties in new product-oriented measurements for model verification mentioned in Section 2.1.

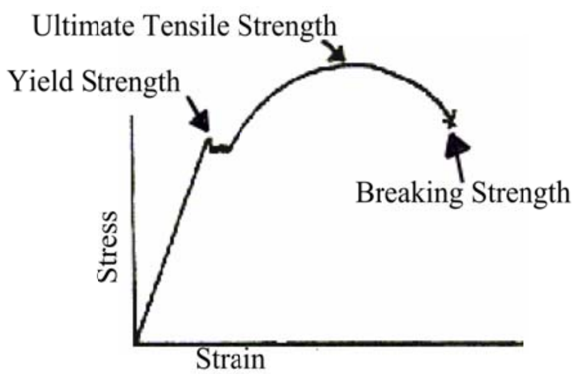

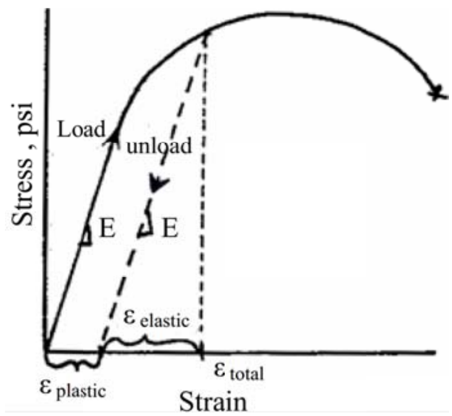

Fig. 2.10: Response of metal to loading stress [24]: (a) Stress-strain curve, (b) Springback.

Touch-trigger probes are usually selected for the measurement of standard geometrical features like holes as mentioned in Section 2.1.1.1, due to their characteristics.

If a hole of small diameter on a deformed sheet metal is manufactured significantly out of nominal position, the probe may crash into the surface instead of stepping into the hole center. If the hole is much larger than designed, missed touches may occur. If the deviation is small, cosine error will be introduced in the results, as mentioned in Section 2.1.1.3.

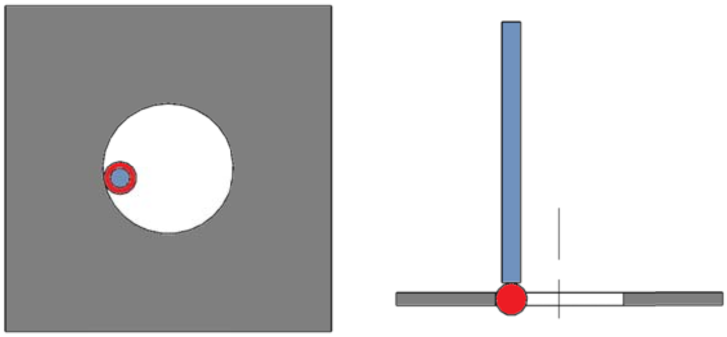

Fig. 2.11: Touch probing features on thin workpiece.

A second problem arises when touch probing a hole in a thin sheet metal (Fig. 2.11). If the surface location differs from the nominal, the spherical probe cannot correctly touch the hole side. A cylindrical probe could be used, but only in the case where probe shaft is exactly normal to the sheet surface. Existing methods for solving this have included taking preliminary sample points on the surface surrounding the features (holes, etc.) to record the actual surface height, and then determining the touch probe path height by offsetting half of the nominal sheet thickness. However, this method is time consuming.

2.3 Multi-Sensor Inspection System

With new developments in production, the requirements for innovative metrology methods and techniques have become increasingly diverse. As the touch probe and the non-contact digitizer each have their own strengths and weaknesses, multi-sensor metrology has been developed which combines them, usually on a CMM. This sensor integration has made it possible to measure almost all kinds of features that may not be obtained by one sensor or the other alone. The high measuring speed of multi-sensor CMMs enables economical on-line inspection [10].

Two kinds of information interaction between the outputs from multiple sensors can be observed in related research, i.e., complementary interaction and synergistic interaction [25]. Complementary information interaction means two or more sensors digitize different features of the same object that are independent of each other, but complement each other. Synergistic information interaction occurs when the data obtained by one sensor (optical sensor) can guide the inspection path of another sensor (touch probe). Different multi-sensor measurement systems have been implemented by researchers, but their research has a different focus and methods.

Reverse Engineering is a field that most multi-sensor inspection systems have been applied to. In reverse engineering, usually no CAD model is available. The non-contact digitizer is employed to measure free-from surfaces due to its high density digitizing characteristic and high digitizing speed, while the touch probe is utilized to measure features that require low uncertainty and ones that cannot be obtained by the optical sensors due to visibility constraints, such as deep holes. Research of [26], [27] and [28] are examples of this application. Their multi-sensor systems work in a complementary way. Research of Bradley et al. [26] focused on feature extraction and fitting. The laser scanner was used to measure free-form surface patches, and the surface patch boundaries were obtained by the touch probe. The patch boundary data was used to segment the free-form surface data into patches. B-spline curve and surface representation of the object was created by modeling both the data sets. The touch probe was moved manually which may cause cosine error. Sladek etc. [27] combined a structured light vision system and a touch probe. The main part of the paper was about working process of the vision system and segmentation of the points digitized by it. Features that needed to be touch probed were determined by the segmentation results, either for lower uncertainty result or compensating the measurement capability of the vision system. Details on creating the touch probe inspection path and common coordinate system were not mentioned. In Xie et al.'s research [28], a one-axis rotary table was used for measuring the object from different views. Inspection planning of the touch probe was not mentioned either.

Carbone et al. [29] and Shen et al. [30] also concentrated on reverse engineering, but they combined the touch probe and the vision system in both complementary and synergistic ways. Carbone et al. first used the scanner data to create a rough CAD model that was then used as guidance for touch probing inspection. The touch probe inspection path was planned using predefined inspection plan functions available in the CMM software. Touch probe measurements were iterated until the deviations between the points on the rough CAD model and those obtained by the touch probe are minimum. Finally, a CAD model was constructed with the data from both sensors. In Shen's research, much effort was put into calibration of the vision system, and a number of algorithms were developed to fuse and extract data from the visual images. Although planning the inspection touch probing points for geometric features based on the complete feature information extracted from the data of vision system was mentioned, details were not covered in the paper.

Another field that attracts attention of researchers is inspection planning, in which the scanner and the touch probe work in a complementary way. Sensor selection for measurement of different features and inspection path planning are the main focuses in this field. Studies of Mohib et al. [31] and Zhao et al. [32] belong to this field. In Mohib's research, a knowledge-based system was employed for sensor selection. Sensor type was selected based on three factors: tolerance specifications, whether the feature is external or internal, and feature dimensions (shape, size, etc.). Order of inspection tasks was determined by considering it as a travel salesperson problem. Each task was treated as a city. The links between them were the travel distances between cities, which were the time spent in moving from one feature to another during inspection. The goal was to minimize the total non-digitising time. Knowledge-based method for sensor selection was also utilized in Zhao's research. Moreover, three issues were fixed for laser scanner inspection planning: view angle calculation, scanner elevation determination, and scan path generation.

Nashman et al.'s research [25] is unique compared with the applications mentioned above. Their system was synergistic inspection based on the condition that no CAD model or planned inspection path was available, and no human operation was involved. The camera captured both the feature (edge etc.) of the object and the touch probe stylus. Algorithms were implemented to extract feature information and probe stylus from the captured images. The distance between the point to be measured and the probe was calculated by sum of absolute differences correlation algorithm and updated in every processing cycle. The touch probe inspection path was guided during the whole measurement by the camera without using CAD model. The camera used the room light as the light source, which may produce inaccurate results.

The concept of the developed multi-sensor inspection system in this thesis is similar to that of Nashman's research. The motivation of our research is to solve the problem mentioned in Section 2.2 more efficiently. The blue LED structured light scanner and the touch-trigger probe work in a synergistic way. However, the CAD model of the workpiece is available in this thesis, as it is needed for creation of the nominal inspection program. The structured light scanner used in this thesis work is more accurate and was calibrated with respect to the CMM.

2.4 Extrinsic Calibration of the Scanner

There are both intrinsic and extrinsic parameters of a scanner. As the intrinsic parameters of the blue LED scanner was calibrated by the manufacturer during production, only extrinsic parameters need to be calibrated. To use the scanner data to guide the touch probe inspection path, the scanner data and the touch probe data need to be transformed into a common coordinate system. In this thesis, the LCS of the scanner was transformed to the Machine Coordinate System (MCS) of the CMM. This process is extrinsic calibration of the scanner. A calibration target is usually needed for scanner calibration. Zhang et al. in [21] used a red/blue flat checkerboard. Xie et al. in [33] designed a planar target with square patterns (Fig. 2.12). In this thesis, an in-house designed angled slot target was employed.

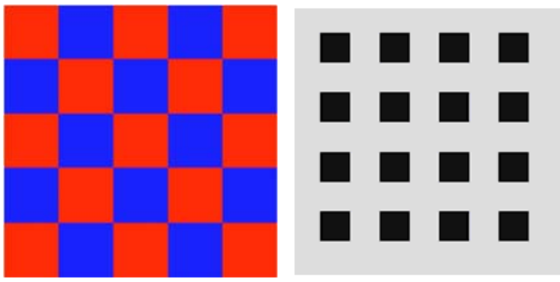

Fig. 2.12: Calibration Target [21],[33]: (a) Red/blue flat checkerboard, (b) Planar target with square patterns.

2.5 Multiple-Orientation Scanning and Coordinate System Registration

There are three ways to measure a 3D object from different orientations with the scanner: rotating the object, moving and rotating the sensor, and utilizing fixed imaging system with multiple cameras [15]. No matter which method is employed, point clouds obtained at different positions and orientations need to be transformed into a common coordinate system. Therefore, the relative position between the scanner and the object needs to be recorded for each position. This process is called coordinate system registration. For the method of sensor movement, approaches for determining the relative position include but are not limited to: (1) Mounting the sensor on a precise mechanical device, the position of which is provided (Fig. 2.13(a)). (2) Optical tracking of the position and orientation of the sensor using reference target on the sensor frame (Fig. 2.13(b)). (3) Measurement of markers accurately fixed in the object field.

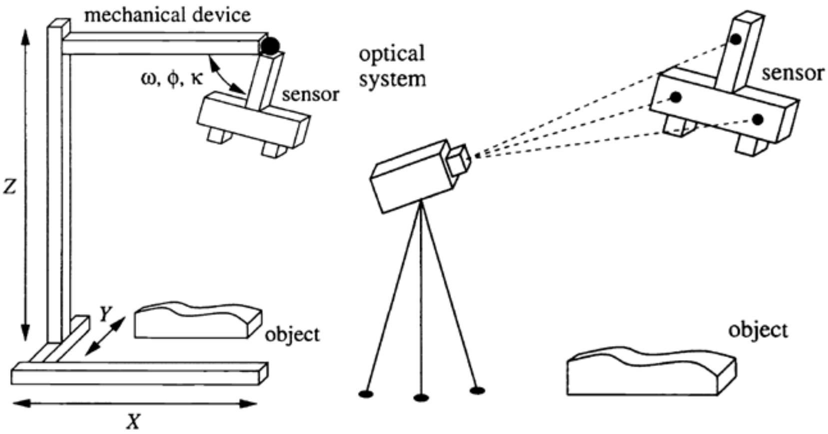

Fig. 2.13: Approaches for determining sensor position [34]: (a) Precise mechanical device, (b) Optical tracking of sensor.

As the blue LED sensor used in this thesis is heavy (1.35 kg) compared with the carrying capacity of the gravity counterbalance spring of the CMM, the method of rotating the object was used instead of rotating the sensor. In most literature, a one-axis accurate mechanical rotary device is used to rotate the object [9],[28],[35]. It has high precision, but the cost is high and it is sensitive to room temperature change. Moreover, its application is limited to cylindrical objects. In this thesis, a lightweight two-axis rotary table was designed for scanning 3D features from different views. Three tooling spheres were mounted on the rotary table for coordinate system registration.

2.6 Rigid Body Errors of CMM

For orthogonal CMMs, the MCS is a Cartesian coordinate system. If no structural error exists, each carriage of the CMM should only move along its axis and the moving direction of the three carriages should be perpendicular to each other. However, no machine is perfect, and there is always structural error. In fact, extraneous motion occurs when the carriage is trying to move only in one dimension. The motion is described as rigid-body kinematics, assuming that the carriage is rigid during motion. Based on that, each carriage has three translational motions (scale along its moving axis and straightness in the other two axes) and three rotational motions (roll, pitch, and yaw) corresponding to its six degrees of freedom (Fig. 2.14). Each of these parameters is a function of axis position. In addition, there are three squareness errors between each two axes [10].

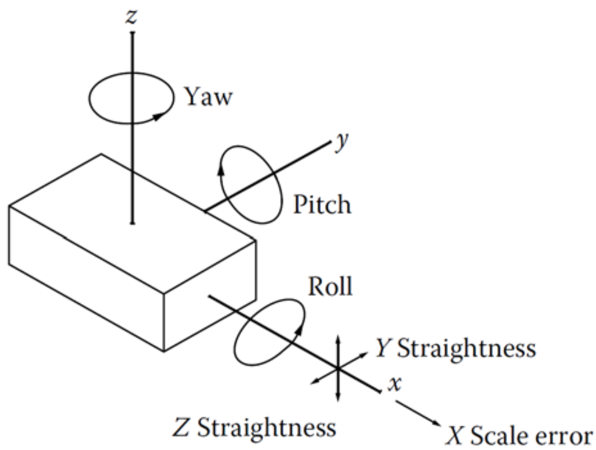

Fig. 2.14: Schematic of error parameters for the *x* axis [10].

Squareness error occurs when any two axes of the coordinate system is out of square [10]. As shown in Fig. 2.15(a), different measurement results can be obtained when measuring the same ball bar length in square and out-of-square coordinate systems. The XY squareness error in Fig. 2.15(a) can be expressed as:

$$\begin{cases} L_1 = \sqrt{x_1^2 + y_1^2}, L_2 = \sqrt{x_2^2 + y_2^2} \\ \varphi = \dfrac{L_1 - L_2}{L_1 \cos\theta \sin\theta} \end{cases} \tag{2.5}$$

If the length of the artifact, L_1 , is known, we can obtain φ by measuring its length in the out-of-square coordinate system, L_2 . If the length of the artifact is unknown, the squareness error can be determined by measuring the same artifact in two crossed positions (Fig. 2.15(b)). The XY squareness error in Fig. 2.15(b) can be expressed as:

$$\varphi = \frac{2\left(L_B - L_A\right)}{L_A + L_B} \tag{2.6}$$

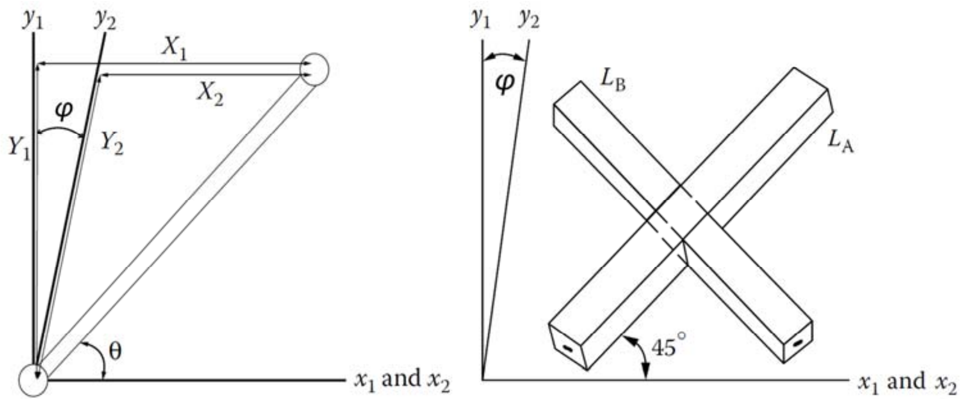

Fig. 2.15: Schematic of XY squareness error [10]: (a) Same ball bar length in square and out-of-square coordinate systems, (b) Estimate method.

Chapter 3

System Architecture

The components of this multi-sensor inspection system (Fig. 3.1) are listed as follows:

Hardware:

- CMM: DEA IOTA-P with retrofitted motors and motion control computer.
- Touch-trigger probe head and probe: Renishaw® PH6/TP6 [36],[37].
- Blue LED structured light scanner: LMI® Gocator 3110 [17].
- Counter card: PCI-QUAD04 four-channel quadrature encoder input board [38].
- Renishaw® AM1 adjustment module [39].
- Designed lightweight 2-axis rotary table.
- In-house designed angled slot calibration target.

Software:

- Siemens NX 9.0 [40].
- Mitutoyo GEOMeasure 3000 DMIS interpreter software [41].
- Geomagic Qualify 12 3D reverse engineering software [42].

- Developed software.

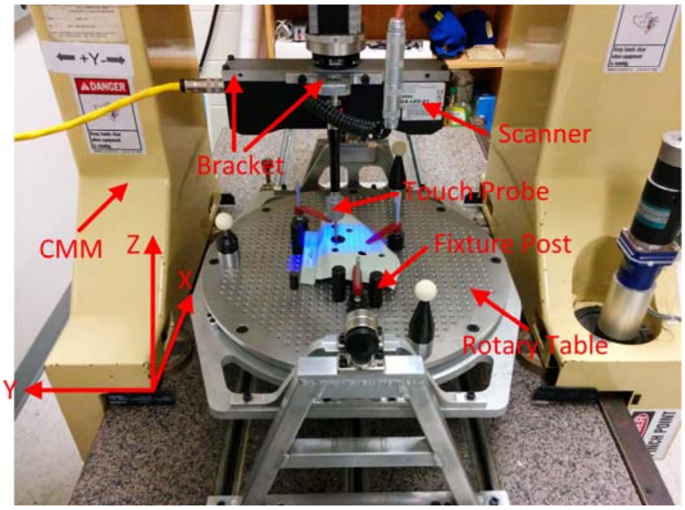

(a)

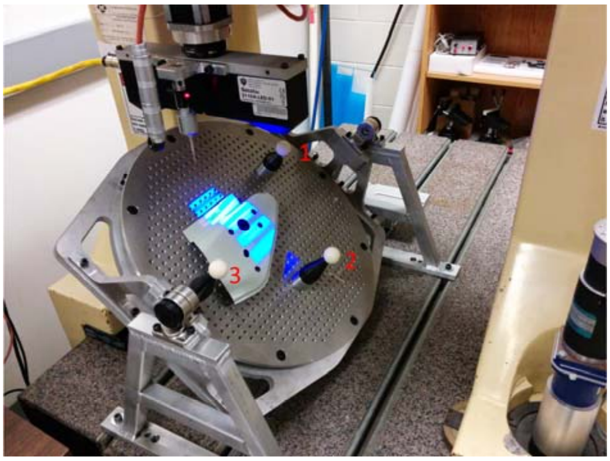

(b)

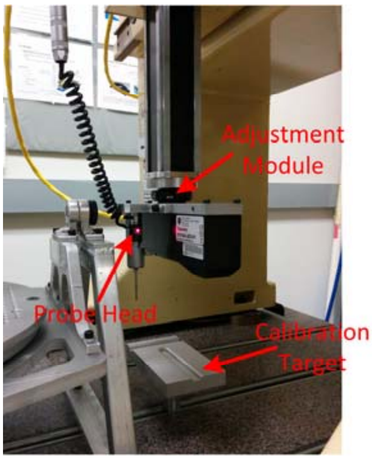

(c)

Fig. 3.1: Multi-sensor system configuration: (a) Horizontal, (b) Oriented, (c) Scanner calibration target.

The scanner and the touch-trigger probe are both affixed to the CMM using designed brackets (Fig. 3.1(a), Appendix A.1, A.2). Two Renishaw® AM1 adjustment modules were used for adjusting roll, pitch, and yaw angles of the scanner and the calibration target that is used for extrinsic calibration of the scanner (Fig. 3.1(c), Appendix A.3). Details are covered in Chapter 4. The designed lightweight 2-axis rotary table is for use with surfaces with non-vertical normal directions. The design procedure is described in Chapter 6. For the DEA IOTA-P CMM used in this thesis, the volumetric roll/pitch/yaw errors and the straightness errors were negligible. Using a ball bar (Fig. 3.2), the static XY squareness error was determined to be 8.073×10^{-4} rad with the "crossed position" method as mentioned in Section 2.6. The static YZ and ZX squareness errors were 3.947×10^{-5} and 1.468×10^{-4} rad respectively. Both linear displacement errors in each axis and squareness errors between axes were compensated by CMM software. The probe stylus was equipped with a 2.5 mm diameter spherical ruby tip. It was qualified by taking five points (one on the top, four quadrant ones on the equator) on a 25.0009 mm diameter precision sphere (Fig. 3.3). The parameters of the blue LED scanner are shown in Tab. 3.1.

Fig. 3.2: Ball bar artifact.

Fig. 3.3: Renishaw® probe qualification sphere.

Measurement Range (mm)	Near Field of View (mm)	Far Field of View (mm)
100	60 × 105	90 × 160
Resolution Z (mm)	Resolution XY (mm)	Scan Rate (Hz)
0.035 – 0.108	0.090 × 0.100 – 0.150 × 0.160	Up to 5

Tab. 3.1: Property parameters of the blue LED scanner.

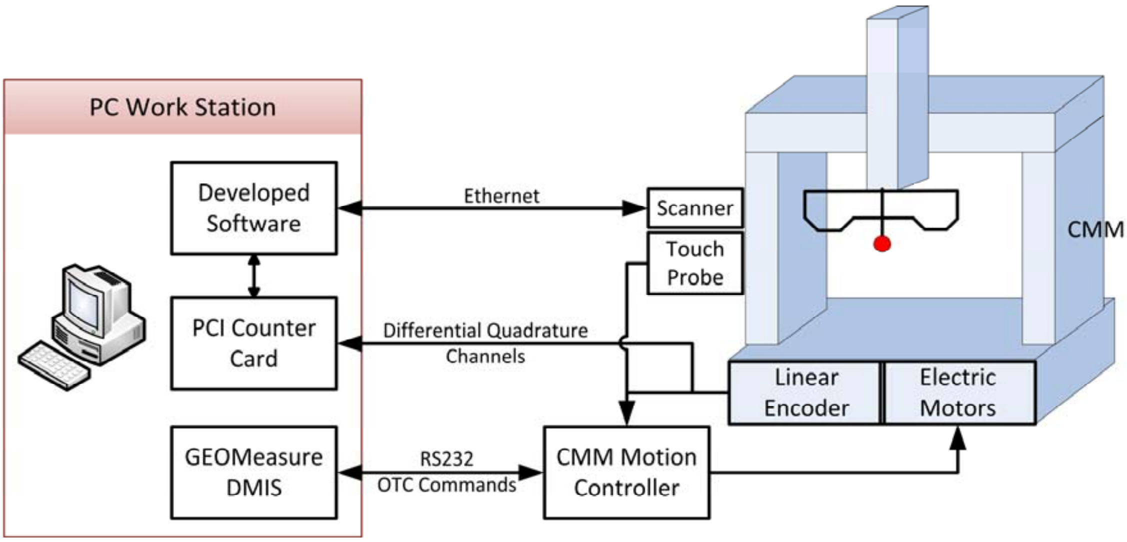

Fig. 3.4: Connection between components of the system.

The connection between the components is illustrated in Fig. 3.4. The counter card embedded in the PC work station was used to capture the CMM scale readings from the CMM linear encoder. Software in programming language C for interacting with both the scanner and the counter card was developed based on Gocator SDK [17] of the scanner and Universal Library [38] of the counter card. The software communicated with the scanner through Ethernet. Siemens NX 9.0 was utilized to create nominal touch probe inspection program from the CAD model. Mitutoyo GEOMeasure was employed for running the adjusted touch probe DMIS inspection program, sending OTC commands to CMM motion controller (OTC 5000C motion control unit), and receiving measurement data from the CMM. Scanner point clouds obtained from oriented part inspection (Chapter 7) were processed and compared using Geomagic Qualify 12.

Chapter 4

Extrinsic Calibration of the Scanner

The point cloud and feature fitting result obtained from the scanner are in LCS. As the scanner is mounted on an external device, CMM, and moving with it, the extrinsic parameters of the scanner have to be calibrated for setting up GCS. Moreover, to use the scanner data to guide the touch probe measurement path, the scanner and the touch probe data need to be transformed into a common coordinate system. In this thesis, the LCS of the scanner was transformed to the MCS of the CMM. To accomplish this, an in-house designed angled slot calibration target was utilized (Fig. 4.1). It is a 160 × 90 × 20 mm^3 square piece with two perpendicular 4.6 mm deep slots, each of which has a pair of symmetric 30° angled edge planes. The slots are 110 mm and 90 mm long respectively. The width of the edge plane is 3.67 mm. The flatness, measured by taking 30 sample points across the top of the target, was 24 µm.

The goal of the calibration process is to obtain the Homogeneous Transformation Matrix (HTM), $HTM_{LCS \rightarrow MCS}$, expressed as:

$$HTM_{LCS \to MCS} = \begin{vmatrix} R_{LCS \to MCS} & T_{LCS \to MCS} \\ 0 \quad 0 \quad 0 & 1 \end{vmatrix} \tag{4.1}$$

As can been seen, there is a rotation matrix and a translation vector in the matrix. During calibration, the LCS of the scanner was first rotated to align its axes with those of the CMM MCS. Then the LCS was translated to align its origin with that of the CMM MCS.

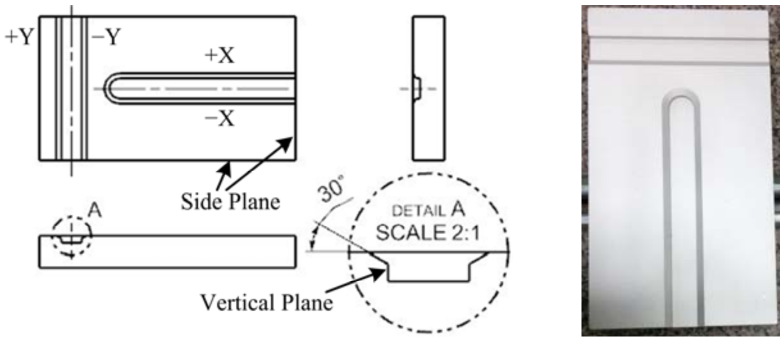

Fig. 4.1: Calibration target: (a) Drawing, (b) Machined part.

Angular misalignments between the axes of the scanner LCS and the CMM MCS were mechanically minimized first. The calibration target was first aligned with the CMM by touching probing its slots and top plane. The scanner was then adjusted to align with the target by scanning the target. For adjusting the roll, pitch, and yaw angles of the calibration target and the scanner, two Renishaw® AM1 adjustment modules were used (Appendix A.3). The angles were adjusted with adjusting capstans and screws of the module. To adjust the target, one adjustment module was mounted beneath it (Fig. 4.2(a)). To mount the target and the module on the CMM granite table, an aluminum collar was designed (Appendix A.4), in which the shank was fixed with two set screws 90° apart from each other. Finally, the aluminum collar was fixed on the granite table with a T-nut and a hex bolt (Fig. 4.2(b)). Using touch probing, the top plane of the target was adjusted to be horizontal, and the long slot to be aligned with the CMM Y axis. Another AM1 module was mounted between the scanner and the CMM Z axis (Fig. 4.2(c)). It was mounted on the scanner with a designed bracket (Appendix A.2) and into the CMM Z axis with a shank and two set screws. The scanner was adjusted to align with the top plane of the target, and its Y axis with the long slot.

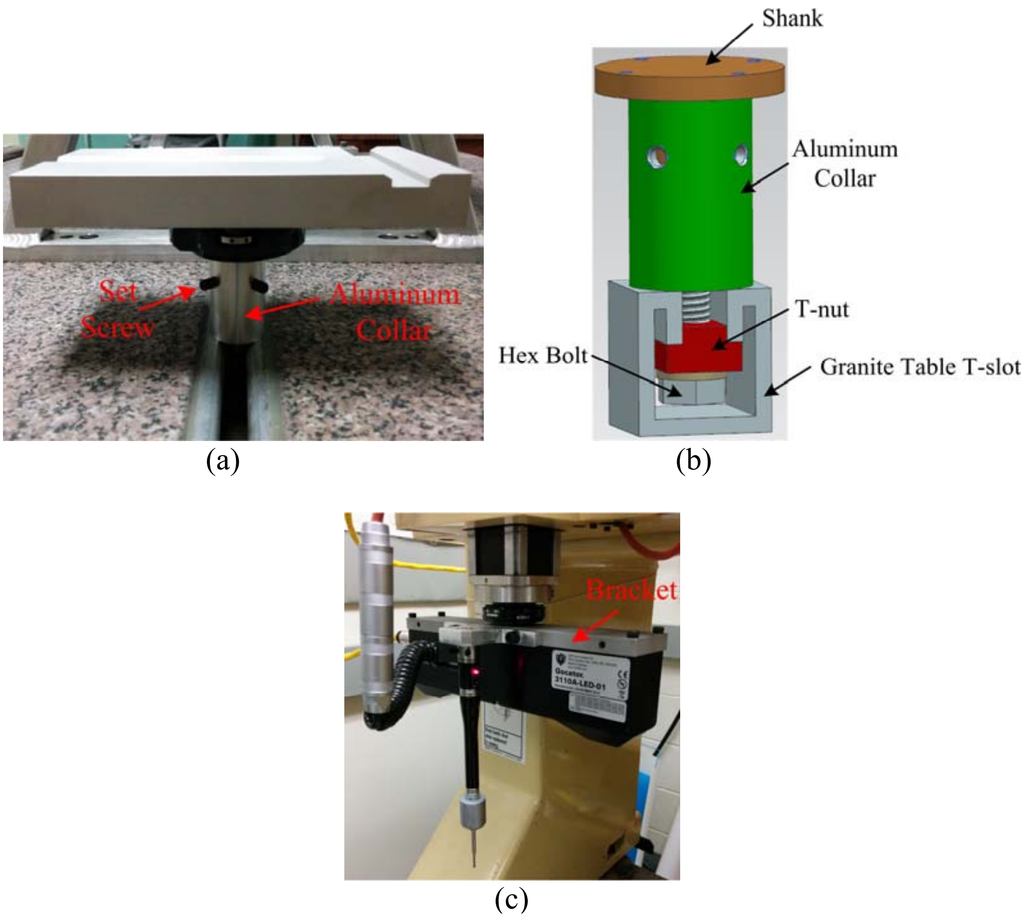

Fig. 4.2: Calibration target and scanner mounted with Renishaw® AM1 adjustment module: (a) Target and adjustment module, (b) Schematic of mounting the target on the CMM granite table, (c) Scanner and adjustment module.

Residual angular misalignments between the axes were corrected mathematically by the obtained rotation matrix $R_{LCS \to MCS}$. The translation vector $T_{LCS \to MCS}$ was also derived with the developed mathematical algorithm to align the origins of LCS and MCS. To derive $HTM_{LCS \to MCS}$, the top plane, the −X and +X 30° angled edge planes of the long slot, and the +Y and −Y 30° angled edge planes of the short slot were all touch probed and scanned to obtain data in the CMM MSC and the scanner LCS respectively. The acquired data were used to transform between LCS, MCS, and the constructed calibration Target Part Coordinate System (TPCS). Detail of the algorithm is described in reference [43]. The translation vector, $T^{'}_{LCS \to MCS}$, derived directly from the algorithm doesn't consider the instantaneous CMM (scanner) position. The final translation vector can be expressed as:

$$T_{LCS \to MCS} = T^{'}_{LCS \to MCS} + \left(P_{CMMi} - P_{CMMc}\right) \tag{4.2}$$

where P is a column vector consisting of X, Y, and Z coordinates. P_{CMMi} is the instantaneous compensated scale readings of the CMM, and P_{CMMc} is the compensated scale readings of the CMM when the calibration target was scanned during calibration.

For scanning the top plane and the angled edge planes, C program was developed with Gocator SDK of the scanner. The scanner was moved to the same spot over the target each time, so that the light exposure and the active area for each feature could be predefined. Exposure determines the camera and light on-time. The active area is the selected region within the maximum field of view that is used for 3D data acquisition. The scanner data of all the planes can be collected by running the program only once.

For touch probing, the challenge was to measure the angled edge planes, as there is slight dimensional deviation in the machined part from CAD model. Deviation can be noticed when using the side planes as the datums (Fig. 4.1), for the probe was sliding on the edge planes when touching them. Therefore, the vertical planes of the slots were used as the datums instead. To construct the datum reference frame, the top plane, the −X vertical plane of the long slot, and the –Y vertical plane of the short slot were all touch probed. Their positions and normal directions were used to set up the reference frame. In that frame, the top plane and the four angled edge planes were finally measured. The obtained data was transformed back to CMM MCS and utilized to derive $HTM_{LCS \to MCS}$.

Chapter 5

Multi-Sensor Synergistic Inspection

The multi-sensor blue LED scanner and touch-trigger probe inspection system takes advantage of the high digitizing speed of the scanner and the low uncertainty of the touch-trigger probe. In this inspection system, after the extrinsic calibration described in Chapter 4, features, such as holes and slots, are first measured with the blue LED scanner. The approximate geometric and dimensional properties of features obtained from the scanner are then used to adjust the nominal tactile DMIS inspection program created from CAD geometry. Finally, the features are touch probed with lower uncertainty using the adjusted DMIS program. The workflow is illustrated in Fig. 5.1. An automotive sheet metal part was measured with this multi-sensor approach.

5.1 Nominal CAD Touch Probe Inspection Program

As the relative position between the holes on the fixture table was known, the fixture posts and the sheet metal part were constructed in CAD model (Fig. 5.2). As mentioned in Chapter 3, the nominal DMIS touch probe inspection program was created from CAD model using Siemens NX 9.0. In this program, the teach point was first touch probed, and the coordinate system was translated from the MCS to it. In this way, the Part Coordinate System (PCS) is constructed. The teach point is a reference point that can be a point on the part or center of a fixture post. The coordinate system transformation was all performed in DMIS program. As the position tolerance is not specified in the engineering drawing (Fig. 5.2), the fixture posts here are for locating the part, but are not used as datum targets. Therefore, they do not need to be measured to construct a datum reference frame. A datum reference frame consists of three mutually perpendicular intersecting datum planes and constrains the six degrees of freedom of the part. The part has a minimum of three contact points with the primary datum feature, two with the secondary datum feature, and one with the tertiary datum feature. In fact, sheet metal parts are usually thin and consist of free-form surfaces, so holes or slots on them are often designed as the secondary or tertiary datum rather than side surfaces. When a position tolerance is specified, the datums need to be measured to construct the datum reference frame, and a new PCS will be constructed according to it.

After measuring the teach point and the datum features (if needed), the touch probe proceeded to measure the features (holes, slots, etc.) of the part that need inspection.

5.2 Scanner Inspection

5.2.1 Scanner Inspection Path and Scanner Parameters

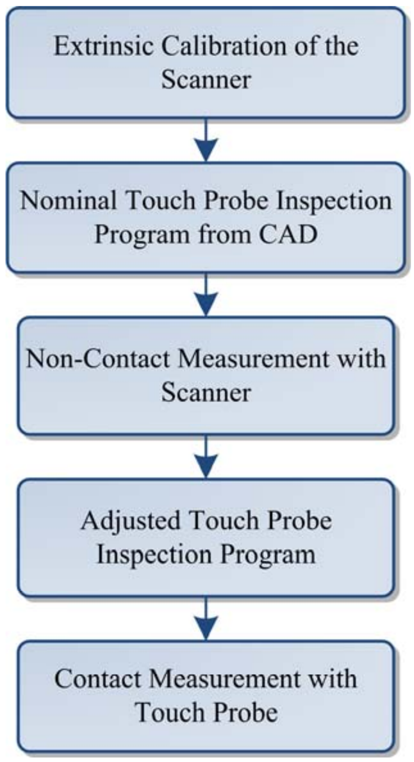

Fig. 5.1: Workflow of multi-sensor inspection system.

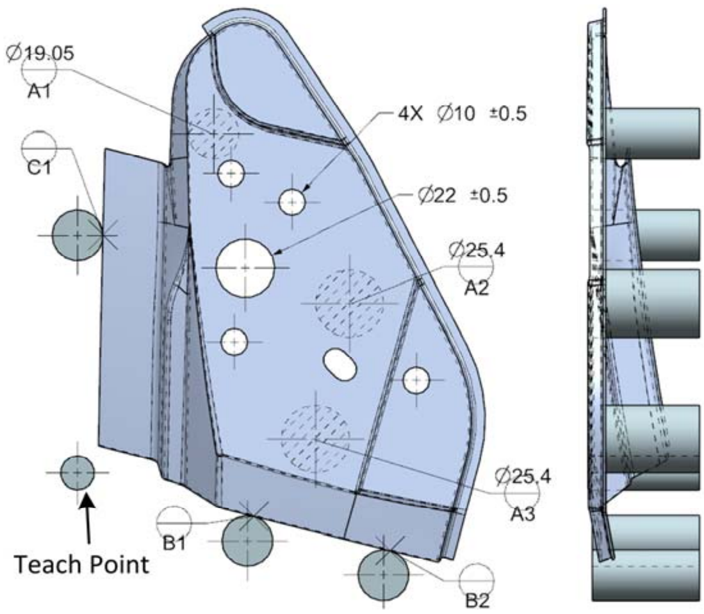

Fig. 5.2: Sheet metal part and fixture posts.

During scanner inspection, the teach point was first scanned by manually moving the scanner over it. The position of the teach point was then recorded and transformed from the LCS to the GCS of the scanner. It can be expressed as:

$$P_{GCS} = R_{LCS \to GCS} \cdot P_{LCS} + P_{CMM} \tag{5.1}$$

where P_{CMM} is the compensated scale readings of the CMM, $R_{LCS \to GCS} = R_{LCS \to MCS}$. The axes of GCS are parallel to those of MCS. The position of the CMM is taken into account in GCS, as the scanner has to move with the CMM to overcome its field of view limitation.

Following that, the nominal GCS positions of the features and datums (if needed) to be measured were obtained from the CAD model based on the GCS position of the teach point. The scanner was then moved automatically to the features using DMIS program in GEOMeasure, taking snapshots, and collecting the data. Software in C for interacting simultaneously with the scanner and the counter card was developed based on Gocator SDK [17] of the scanner and Universal Library [38] of the counter card. Measurement tools for 3D feature recognition are offered all inside the scanner and implemented in the developed software. The software was employed to enable the time trigger of the scanner, obtain the scanner measurement data through Ethernet, capture the instantaneous compensated scale readings of the CMM, and process and output the data.

The height of the scanner was adjusted to keep the part in the near view of the scanner (50 mm from the part surface) so that higher resolution could be achieved. The acquisition speed of the scanner depends much on the resolution, the selected active area size, and exposure time. If the resolution is set high, the active area is large, or the exposure time is long, the frame rate of the scanner has to be set low, otherwise the processing blocks will be dropped due to heavy CPU load. In this thesis, the resolution was set to be the highest 0.1 mm. The active area was set to be square, centered at the nominal hole position, and 10 mm larger than the nominal hole diameter to collect the points on the surface surrounding the holes. The exposure was set using the "Auto Set" function of the scanner. The frame rate was set as 4 Hz.

In the case where more than one features needed to be measured in one snapshot, the scanner moved to the middle of the features. The active area of each feature was then set automatically in the developed C software based on the nominal GCS positions of the features, and the instantaneous CMM position. For example, the active area for a hole can be expressed as:

$$\begin{aligned} &ActArea.X = CMM.X - HoleX_{nom} - \left(d+10\right)/2 \\ &ActArea.Y = -\left(CMM.Y - HoleY_{nom}\right) - \left(d+10\right)/2 \\ &ActArea.Z = -CMM.Z - 32.5 \\ &ActArea.L = d+10,\ ActArea.W = d+10,\ ActArea.H = 20 \end{aligned} \tag{5.2}$$

where all the values are in mm, $\left(ActArea.X, ActArea.Y\right)$ is the upper left corner of the area on X-Y plane, $CMM.I, I = X, Y, Z$ is the instantaneous compensated scale reading of the CMM, $\left(HoleX_{nom}, HoleY_{nom}\right)$ is the nominal GCS position of the hole, and d is the diameter of the hole. There is a minus sign before $\left(CMM.Y - HoleY_{nom}\right)$, because the LCS of the scanner is left-handed. There is also a minus sign before $CMM.Z$, because the Z coordinate of the CMM highest positon is 0. The value 32.5 is to ensure the whole feature is included in the active area in Z direction. This value is related to the Z measurement range and clearance distance of the scanner (Fig. 2.7), and can be adjusted as needed. The length, width, and height of the active area were set as well.

5.2.2 Compensation of Counter Card Reading

The scale readings of the CMM need to be recorded each time the scanner is moved to a new location along with the CMM, so that scanner data can be transformed from LCS to MCS or GCS. The counter card was used for this purpose. The counter card captures the scale readings of the CMM that are later compensated by software considering the CMM rigid body errors mentioned in Section 2.6. As mentioned in Chapter 3, the volumetric roll/pitch/yaw errors and the straightness errors of the CMM were negligible. Only the linear displacement error in each axis as a function of axis position and the squareness errors between the axes need to be compensated. They are stored in an error map. According to reference [10], the compensation for each axis can be expressed as:

$$\begin{aligned}\Delta X &= \delta_x\left(X\right) - Y'\varphi_{xy} - Z'\varphi_{zx} \\ \Delta Y &= \delta_y\left(Y\right) - Z'\varphi_{yz} \\ \Delta Z &= \delta_z\left(Z\right)\end{aligned} \tag{5.3}$$

where $\delta_i\left(I\right), I = X, Y, Z$ is the linear displacement error, φ is the squareness error in radians, Y' can be expressed as (same for Z'):

$$\begin{aligned}ucY &= \mathrm{Min}\left(YMaxPosition, \mathrm{Max}\left(Y, YMinPosition\right)\right) \\ Y' &= ucY - YMinPosition\end{aligned} \tag{5.4}$$

where $YMaxPosition$ and $YMinPosition$ are the compensation range of the axis position. In order to compensate the readings, ΔX, ΔY and ΔZ should be added to the measured coordinates.

5.2.3 Scanner Measurement Result

Measurement tools for feature fitting are offered all inside the sensor. Corresponding functions are provided in Gocator SDK and employed in the developed C software. For hole feature recognition, there are three phases: Search, Measure, and Filter [16]. In search phase, the tool searches for coarse edge data and carries out a rough fitting of the hole feature. The data within the measurement region are employed to evaluate the part orientation. In measure phase, more strict edge detection is performed to accurately determine the hole edge. Outliers and noise are rejected in this step. The set of refined edges is then used to locate and inspect the feature. Finally, in filter phase, the detected location and size of the hole are decided to be valid or not by comparing them with the nominal and tolerance of the hole size. The nominal radius and its tolerance were predefined in the developed C software according to engineering drawing. The measurement region parameters need to be set to limit the region in which feature extraction will occur. It was set in the same way as the active area as described in Section 5.2.1, except that it is 4 mm larger than the nominal hole diameter. The actual approximate radii and X, Y, and Z positions of the holes, X, Y, and Z positions of the teach point and datum features (if needed), and the point cloud data in the active areas were output from the software and transformed to the CMM MCS (Eqn. (5.5)).

$$P_{MCS} = HTM_{LCS \to MCS} \cdot P_{LCS} \tag{5.5}$$

As mentioned in Section 5.1, in touch probe inspection, the teach point is first measured and the CMM MCS is translated to it. Accordingly, the scanner data need to be transformed from MCS to PCS, the origin of which is the teach point (Eqn.(5.6)).

$$\begin{aligned} P_{PCS} &= HTM_{MCS \to PCS} \cdot P_{MCS} \\ HTM_{MCS \to PCS} &= \begin{bmatrix} 1 & 0 & 0 & -X_{TP}^{MCS} \\ 0 & 1 & 0 & -Y_{TP}^{MCS} \\ 0 & 0 & 1 & -Z_{TP}^{MCS} \\ 0 & 0 & 0 & 1 \end{bmatrix} \end{aligned} \tag{5.6}$$

where $\left(X_{TP}^{MCS}, Y_{TP}^{MCS}, Z_{TP}^{MCS}\right)$ is the coordinate of the teach point in MCS obtained from the scanner. If a datum reference frame needs to be set up, the PCS will be constructed according to it using the measured datum features.

When touch probing a hole in thin sheet metal, a common challenge is to determine the height of the planned touch probe point as mentioned in Section 2.2. With this multi-sensor approach, the average height of surface points within a 1×1 mm^2 square zone adjacent to each planned touch probe hole point was calculated (Fig. 5.3), and offset by half the part thickness to program the touch probe contact.

5.3 Touch Probe Program Adjustment and Inspection

The nominal DMIS program created from the CAD model was adjusted using the scanner data. The coordinates of the planned touch probe hole points were edited based on the approximate radii and X, Y positions of the holes, and the height of the planned hole points obtained from the scanner measurement result. The rest of the program remained the same.

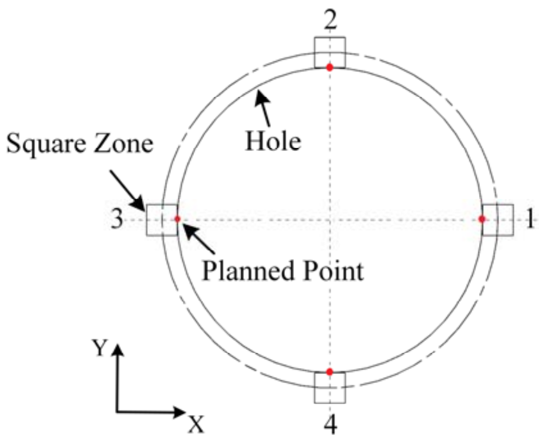

Fig. 5.3: Determination of the height of the planned touch probe point.

In touch probe inspection, the teach point and the datum features (if needed) were measured first to construct the PCS. The coordinate system was first translated from MCS to the teach point. If the datum features are measured to set up a datum reference frame, further transformation is needed. The transformation was all done in DMIS program and performed in GEOMeasure.

When touch probing the holes, iterating process is needed to achieve measurement results of high accuracy, until converged results are obtained. The X and Y positions and radii of the holes were provided by the scanner result for the first measurement. Subsequent measurements were guided by the result of the previous tactile measurement for iterating. The heights of the planned touch probe hole points were always determined by the scanner result.

Chapter 6

Rotary Table Design

In this multi-sensor set up, the scanner is projecting structured light vertically. If the normal direction of the part surface or the axis of the feature to be measured is far from the vertical direction, high uncertainty scanning results will be obtained. At high angles, the features cannot be captured at all by the scanner. Therefore, a lightweight 2-axis rotary table was designed to scan surfaces from different view angles, providing 4th and 5th rotary axes in addition to X, Y and Z axis of the CMM. The rotary table shown in Fig. 6.1 is the final design. It consists of a pair of vertical base supports, suspend hangers, locking hinges, a bottom plate, a round plate and a ring (*Lazy Susan* style) bearing. The vertical base supports are mounted on the CMM granite table through the T-slots using T-nuts. The round plate is mounted on the bearing, providing one rotary axis. The adjustable 10° angle increment locking hinges [44] provide the second rotary axis. Three tooling spheres mounted on the table provide coordinate system registration for different table orientations. During the design process, the dimensions of the parts were determined first, ensuring the rotary table can fit in the volume of the CMM. The forces on the parts were then calculated, and the structure strength was analyzed with Nastran FEA package in

Siemens NX 9.0 [40]. The design was modified in the FEA process, which resulted in original design, welding design, and combined final design. Finally, the strength of key joints was checked.

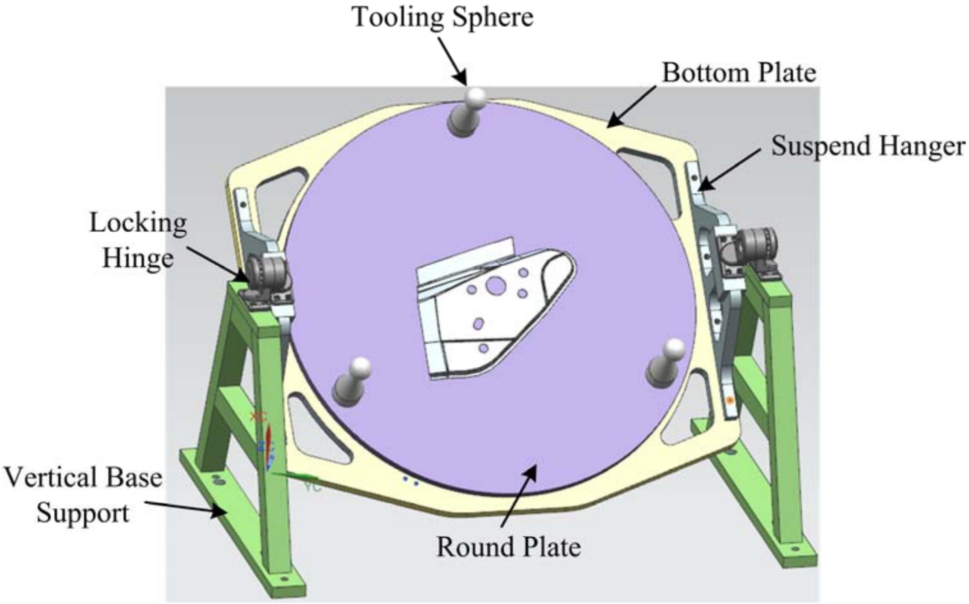

Fig. 6.1: Rotary Table Final Design.

6.1 Dimension Design

The important dimensions of the DEA IOTA-P CMM that need to be considered when determining the rotary table dimension is shown in Tab. 6.1. The CMM axes are illustrated in Fig. 3.1(a).

Item	Value (mm)
Distance between CMM bridges along Y	600.075
Height of the CMM	558.80

Tab. 6.1: Important dimensions of the DEA IOTA-P CMM.

The diameter of the round plate is 460 mm. When designing the distance between the two vertical base supports along the rotary axis of the locking hinges, the thicknesses of the vertical base support, the suspend hanger, and the length of the bottom plate (larger than 460 mm) should be considered. In addition, the CMM air bearings take space between the bridges. Therefore, the rotary axis of the locking hinge was determined to be along the CMM X axis.

6.1.1 Suspend Hanger

The height of the suspend hanger should be larger than that of the part to be measured, so that the center of gravity is lower than the rotary axis of the locking hinge. The suspend hanger should be thick enough to bear the sum of the gravities of the round plate, the bottom plate and the measured part. The top of the suspend hanger should be thick enough to support the hinge base (Fig. 6.2). See Tab. 6.2.

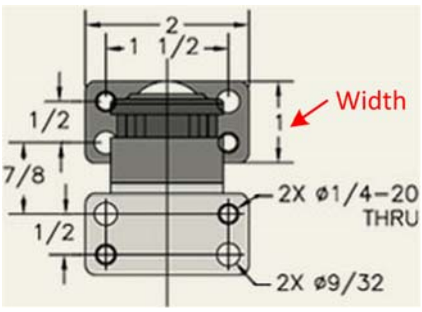

Fig. 6.2: Dimension of the locking hinge (in) [44].

Item	Condition	Conclusion
Height	Height of measured part.	100 mm, larger than height of part for experiment.
Thickness	Width of hinge base, 1 in.	12.7 mm (0.5 in) thick, 25.4 mm (1 in) thick on the top.

Tab. 6.2: Dimension of suspend hanger.

6.1.2 Bottom Plate

The width of the bottom plate should be larger than the diameter of the round plate, and smaller than the distance between the CMM bridges. When designing the length of the bottom plate, the thickness of the suspend hanger and the diameter of the round plate should be taken into account. See Tab. 6.3.

Item	Condition	Conclusion
Width	Distance between bridges, 600.075 mm; Diameter of round plate, 460 mm.	480 mm, $460 < 480 < 600.075$.
Length	Thickness of suspend hanger, 12.7 mm; Diameter of round plate, 460 mm.	528 mm, $460 + 12.7 \times 2 < 528$ 20 mm margin on each side.
Thickness	High rigidity, little bending.	12.7 mm (0.5 in), to be checked by FEA.

Tab. 6.3: Dimension of bottom plate.

6.1.3 Vertical Base Support

The vertical base support should be thick enough to support the weight of the whole assembly and the workpiece, and bear large bending moment. When designing the height, the height of the locking hinge, the suspend hanger, and the thickness and width of the bottom plate should be considered (Fig. 6.3). As the vertical base supports are mounted on the CMM granite table through the T-slots using T-nuts, position of clearance holes on the base needs to be designed. See Tab. 6.4.

6.1.4 Assembly Volume Check

Whether the whole assembly of the rotary table can fit into the CMM is checked in this section.

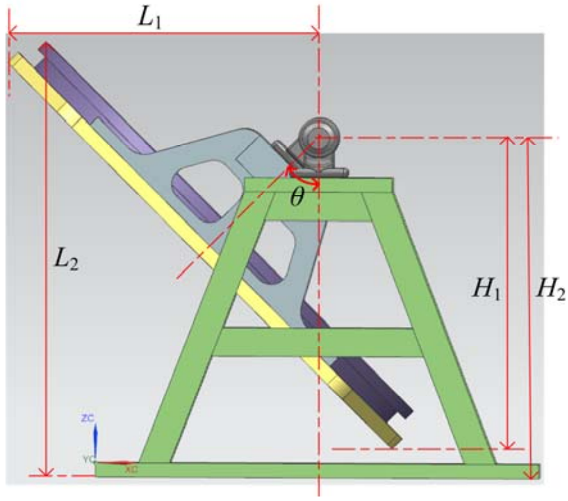

Fig. 6.3: Side view of rotary table assembly and key dimensions.

Item	Condition	Conclusion
Thickness	High rigidity, little bending. Width of hinge base, 1 in.	25.4 mm (1 in) thick.
Height	Height of hinge, 35 mm; Height of suspend hanger, 100 mm; Thickness of bottom plate, 12.7 mm; Half width of bottom plate, 240 mm.	$H_1 = (35+100+12.7)\cos\theta + 240\sin\theta$. When $\theta = 58.3912°, H_{1\max} = 281.807$ mm. $\because H_2 > H_{1\max}$ $\therefore H_{vb} > H_{1\max} - 35 = 246.807$. Set $H_{vb} = 265$ mm.
Holes	Distance between T-slots on the granite table, 174 mm.	Distance between holes is the same as distance between T-slots.

Tab. 6.4: Dimension of vertical base support.

6.1.4.1 Dimension along CMM Y Axis

Dimension of the assembly along CMM Y axis was calculated and compared with the distance between the bridges of the CMM (Fig. 6.3).

$$L_1 = (35+100+12.7)\sin\theta + 240\cos\theta \tag{6.1}$$

When $\theta = 31.6088°, L_{1\max} = 281.807$ mm. 281.807 < 600.075/2 = 300.038.

6.1.4.2 Dimension along CMM Z Axis

The distance between the highest and lowest point of the assembly was calculated and compared with the height of the CMM (Fig. 6.3).

$$L_2 = 230\sin\theta - (35 + 100 - 24)\cos\theta + 35 + 265 \quad (6.2)$$

where 230 is the radius of the round plate, and 24 is the sum of the thicknesses of the round plate and the bearing. The derivative of L_2 is,

$$L_2^{'} = 230\cos\theta + 111\sin\theta \quad (6.3)$$

When $0° < \theta < 90°, L_2^{'} > 0$. Therefore, L_2 keeps increasing with angle θ. When $\theta = 90°, L = 530 < 558.8$.

6.2 Force Analysis

The force imposed on each component was analyzed and calculated in this section. The free body diagram of the whole assembly is shown in Fig. 6.4. N_1 and N_2 are the bearing forces imposed by the CMM granite table on the left and right vertical base supports. G_v, G_s, G_{rp}, G_b and G_p are the gravities of the vertical base support, suspend hanger, round plate (including bearing ring), bottom plate, and the part to be measured respectively. The bearing force can be expressed as:

$$N_1 = N_2 = \left(2G_v + 2G_s + G_{rp} + G_b + G_p\right)/2 \quad (6.4)$$

When considering the round plate, the bottom plate and the suspend hangers as one assembly, the force on the assembly is shown in Fig. 6.5. F_s is the pulling force provided by the locking hinge, and f is the bearing force by the joints between the suspend hanger and the locking hinge. When the table is rotated angle θ, the forces can be expressed as:

$$F_s = \left(G_{rp} + G_b + G_p + 2G_s\right)\cos\theta / 2 \tag{6.5}$$

$$f = \left(G_{rp} + G_b + G_p + 2G_s\right)\sin\theta / 2 \tag{6.6}$$

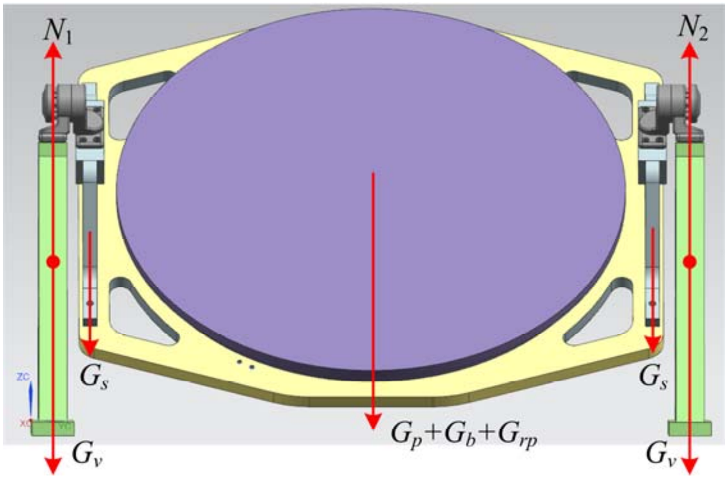

Fig. 6.4: Free body diagram of rotary table assembly.

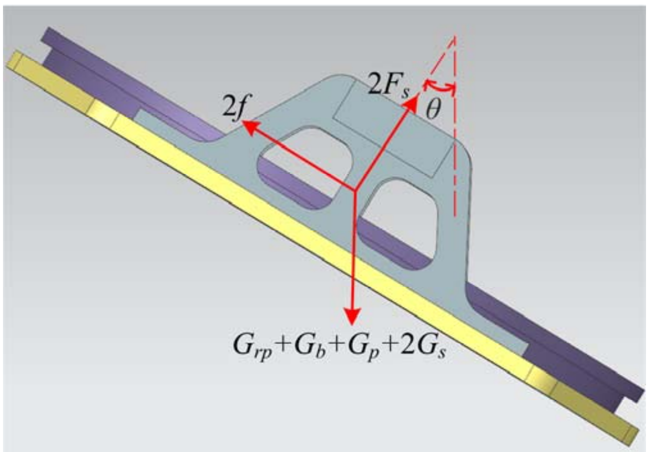

Fig. 6.5: Free body diagram of round plate, bottom plate and suspend hanger assembly.

As can be seen in Fig. 6.6, the round plate and the bottom plate are subject to the gravities of themselves and the measured part, the pulling force provided by the suspend hanger (F_b), and the bearing force by the joints between the suspend hanger and the bottom plate (f_b). When the table is rotated angle θ, the forces can be expressed as:

$$F_b = \left(G_{rp} + G_b + G_p\right)\cos\theta / 2 \tag{6.7}$$

$$f_b = \left(G_{rp} + G_b + G_p\right)\sin\theta / 2 \tag{6.8}$$

The forces on the suspend hanger are presented in Fig. 6.7. It is subject to its own gravity (G_s), the reaction force by the bottom plate and the round plate ($F_b' = F_b$), the bearing force by the joints between the suspend hanger and the bottom plate (f_s), and force f, F_s mentioned above. Force f_s can be expressed as:

$$f_s = f - G_s \sin\theta = \left(G_{rp} + G_b + G_p\right)\sin\theta / 2 \tag{6.9}$$

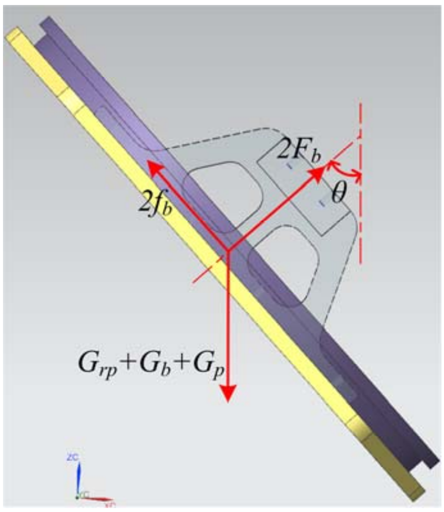

Fig. 6.6: Free body diagram of the round plate and the bottom plate.

As with the vertical base support, it is subject to its own gravity (G_v), compression force F_v, and bearing force $N_{1,2}$ (Fig. 6.8). F_v can be expressed as:

$$F_v = N_{1,2} - G_v = G_s + \left(G_{rp} + G_b + G_p\right)/2 \tag{6.10}$$

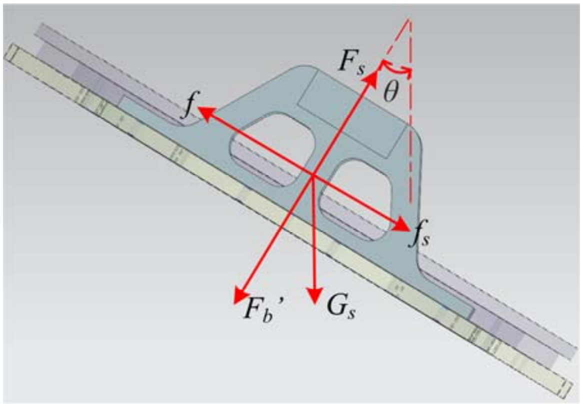

Fig. 6.7: Free body diagram of suspend hanger.

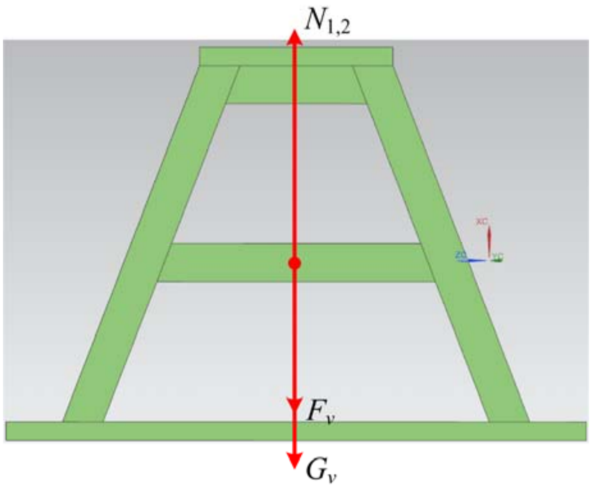

Fig. 6.8: Free body diagram of vertical base support.

6.3 Design Based on FEA

After force analysis, the design was modified based on FEA of the components to reduce the displacement of the components as much as possible. FEA was performed assuming the rotary table was horizontal when the loading forces on the suspend hanger and the bottom plate are the largest (Eqn. (6.5) and (6.7)). The whole design process involved original design, revision of original design, welding design, and final combined design. The main structures of the rotary table and the components that compose the table were not changed. Only the shape and the dimensions of the components, or how they are assembled, were modified.

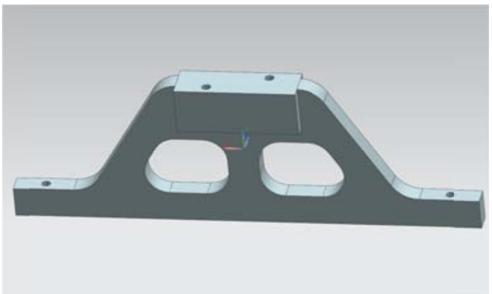

(a)

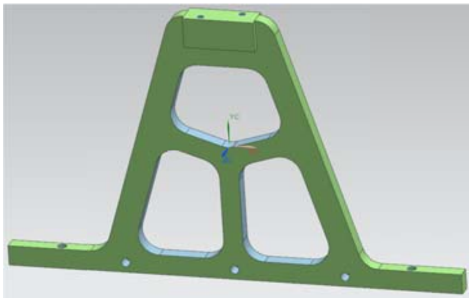

(b)

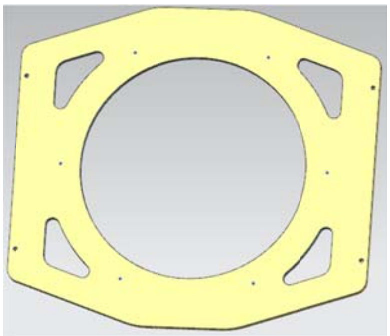

(c)

Fig. 6.9: Original design: (a) Suspend hanger, (b) Vertical base support, (c) Bottom plate.

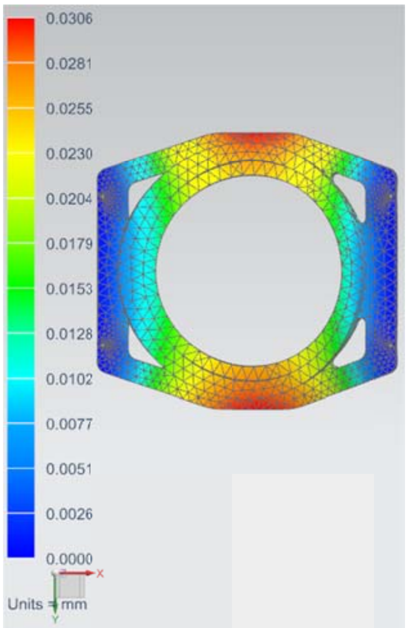

(a)

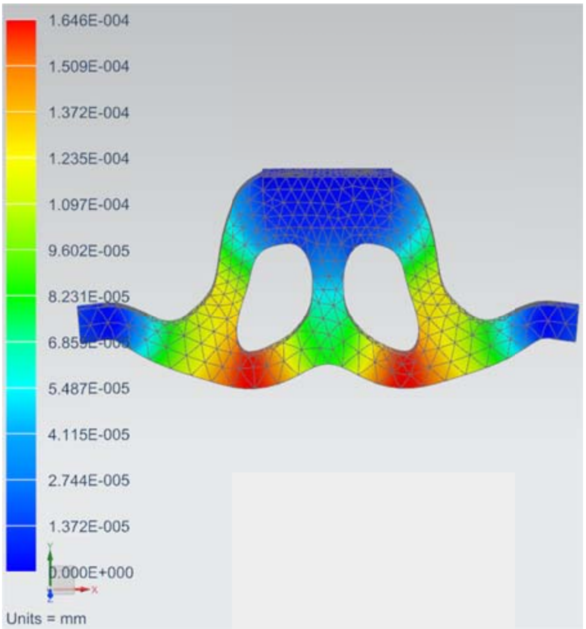

(b)

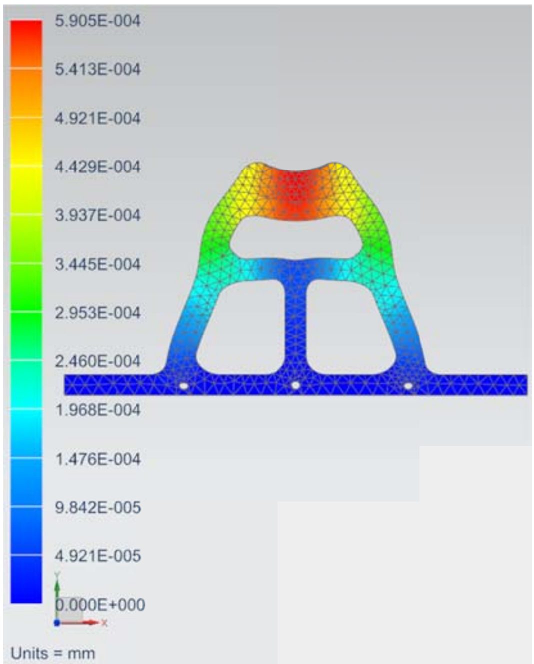

(c)

Fig. 6.10: FEA of original design (displacement): (a) Bottom plate, (b) Suspend hanger, (c) Vertical base support.

6.3.1 Original Design

The three main components of the rotary table in the original design are presented in Fig. 6.9. The thicknesses of the suspend hanger, vertical base support, and bottom plate are 12.7 mm, 14 mm, and 10 mm respectively. The large hollow of the bottom plate is a 332.75 mm diameter hole. The total mass of the assembly is 13.776 kg. Using the forces calculated from Section 6.2, FEA was performed, assuming the mass of the measured part is 7.5 kg, and the result is shown in Fig. 6.10. The ring bearing was added to the CAD model when analyzing the bottom plate, so that the loading area of the force could be selected easily. As can be seen, the maximum displacement of the bottom plate is large (30.6 μm), meaning the bottom plate has low rigidity. This will cause error when merging scanner point clouds obtained from different orientations together. The bottom plate should be designed thicker, and the hollow should be smaller to strengthen the structure. The displacement in the bottom of the suspend hanger below the hollow is large (Fig. 6.10(b)). Holes can be added to the bottom, so that there are more joints between the suspend hanger and the bottom plate. More ribs are needed for the vertical base support to strengthen the structure.

6.3.2 Revision of Original Design

Revision of original design is shown in Fig. 6.11. The vertical base support is thickened to be 15.875 mm (5/8 in). Ribs are added to the hollow part of it. Holes are added to the bottom plate and the bottom of the suspend hanger to strengthen the structure. The shape and the structure of the bottom plate remain the same, except that the hollow hole is reduced to be 312.75 mm diameter, and it is thickened to be 12.7 mm (0.5 in) thick. The total mass of the assembly is 15.184 kg. The FEA result is illustrated in Fig. 6.12. According to Eqn. (6.7) and (6.10), the forces imposed on the suspend hanger and the vertical base support raise because of the increase in the gravity of the bottom plate. However, the displacements of the suspend hanger and the vertical base support decrease as their structures are much stronger. The structure of the bottom plate becomes stronger as well, with 11.2 μm smaller displacement.

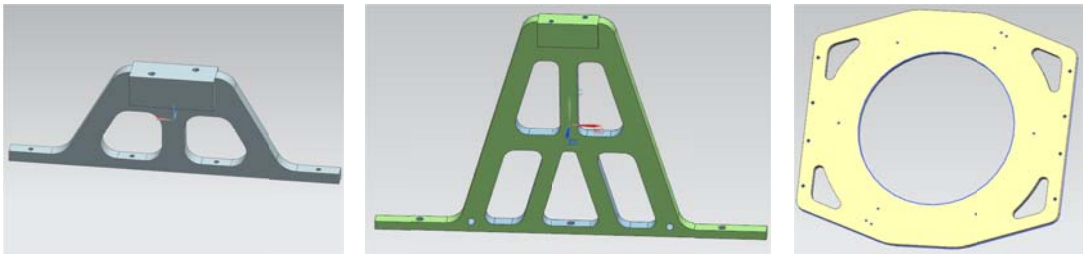

(a) (b) (c)

Fig. 6.11: Revision of original design: (a) Suspend hanger, (b) Vertical base support, (c) Bottom plate.

6.3.3 Welding Design

To reduce the weight of the whole assembly and further strengthen the structure, the components of the table were designed using $1.25 \times 1.25 \times 0.12$ in^3 aluminum square tubes and welding them together (Fig. 6.13). The two suspend hangers and the bottom plate are welded together to strengthen the structure. The total mass of the assembly is smaller compared with previous designs, 12.414 kg. FEA was performed and presented in Fig. 6.14 and Fig. 6.15. As is shown, the maximum displacement of the bottom plate decreases much (6.6 μm smaller than revision of the original design). However, the displacement of the vertical base support increases, but is still small (1.5 μm). Changing the bottom plate from crossing to quadrilateral structure doesn't improve it when the table is horizontal (Fig. 6.15). However, analysis shows that the displacement of the quadrilateral structure is smaller than the crossing one when the table is rotated to a degree, as the quadrilateral structure can bear more shear load. Although the displacement of the bottom plate of the welding design is smaller, it is inconvenient to mount the bearing ring on the bottom plate with screws and washers. Moreover, the welded square tubes may bend after they are cooled down.

6.3.4 Combined Final Design

At last, a design that combines the revision of original design and the welding design was employed. The bottom plate and the suspend hanger of the revision design were used, and the vertical base support was from the welding design. FEA was performed on each part. The maximum displacements of the bottom plate, the suspend hanger, and the vertical base support are 19.4 μm, 0.1 μm, and 1.66 μm respectively. The weight of the whole assembly is 14.342 kg, which is less than that of the revision design. In addition, the bottom plate and the suspend hanger have higher rigidity than those of the original design. Although the displacement of the vertical base support is larger, it is very small and will not have much influence on the performance of the rotary table.

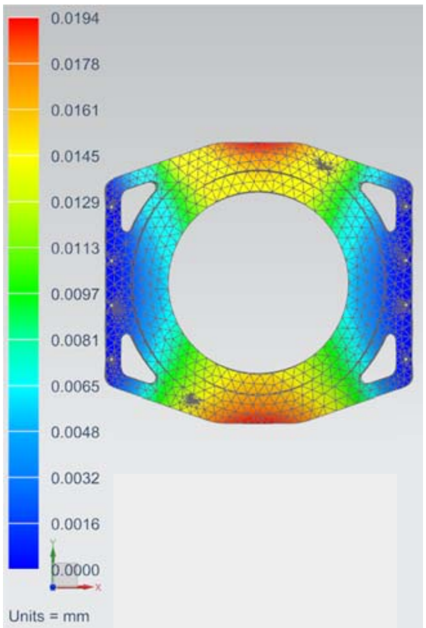

(a)

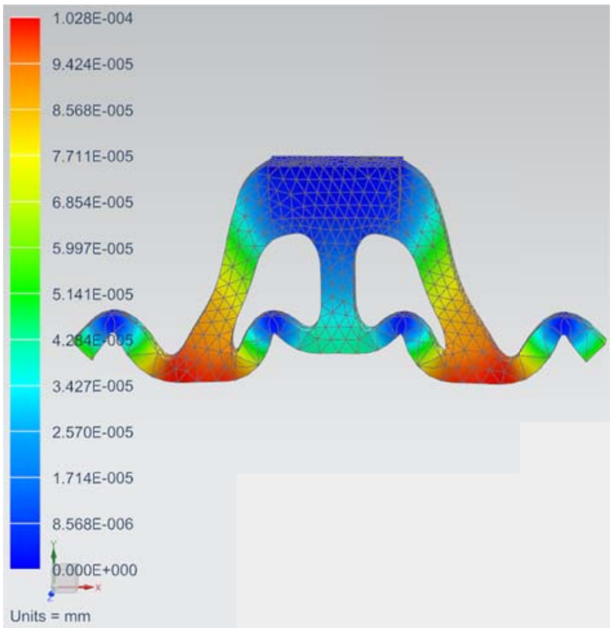

(b)

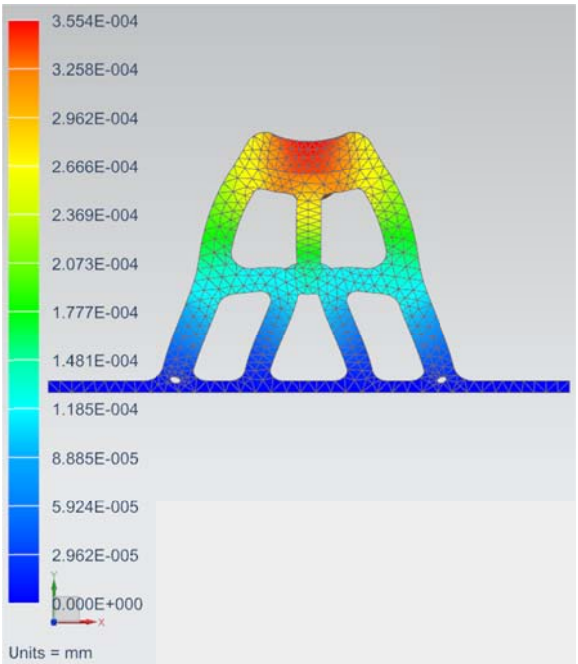

(c)

Fig. 6.12: FEA of revision of original design (displacement): (a) Bottom plate, (b) Suspend hanger, (c) Vertical base support.

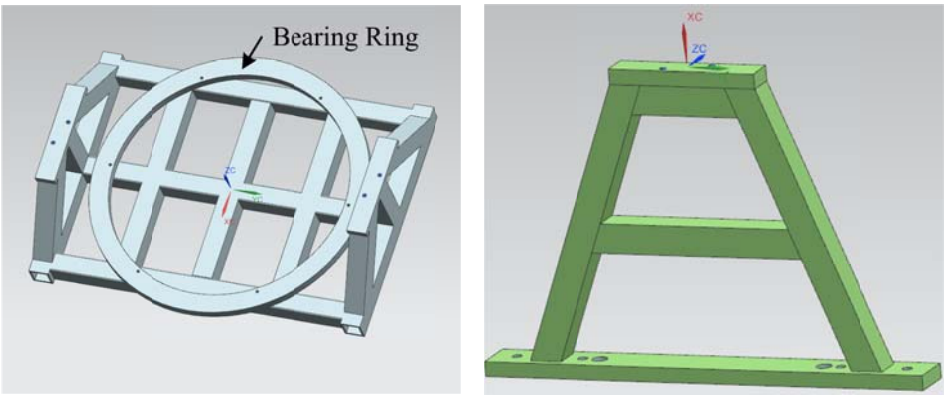

Fig. 6.13: Welding design: (a) Suspend hangers and bottom plate, (b) Vertical base support.

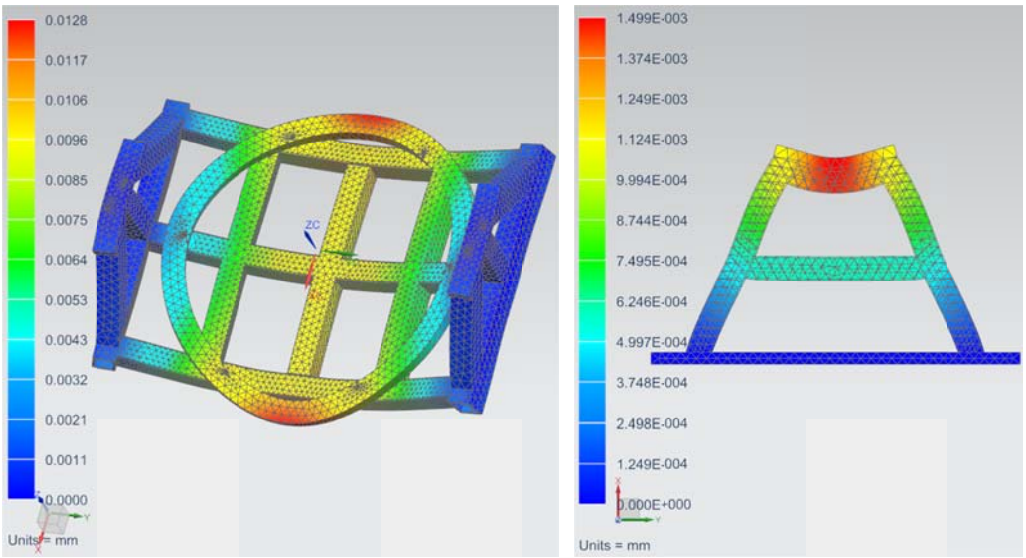

(a) (b)

Fig. 6.14: FEA of welding design (displacement): (a) Bottom plate (crossing structure) and suspend hangers, (b) Vertical base support.

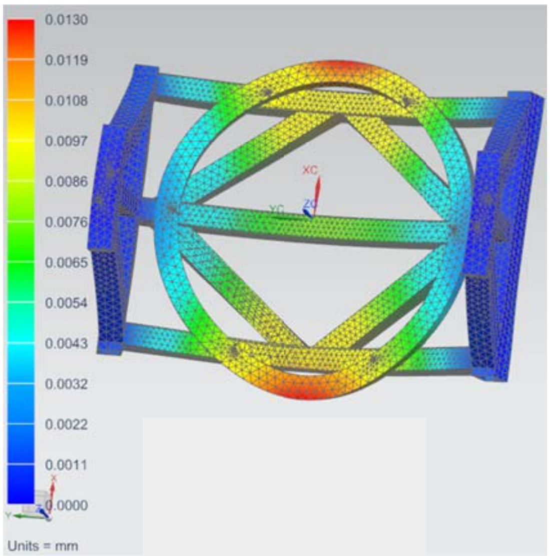

Fig. 6.15: FEA of welding design (displacement): Bottom plate (quadrilateral structure) and suspend hangers.

6.4 Strength Check

In this section, the tensile and shear strength of the screw, the tensile and bearing strength of the suspend hanger, the bearing strength of the bottom plate, and the torque on the hinges were checked.

6.4.1 Strength Check of Screw

The yield strength and shear strength of DIN 912, Class 12.9 socket cap screw are 1100 MPa and 732 MPa respectively [45]. The screws of the same type that connect the locking hinge and the suspend hanger, and the screws of the same type that connect the suspend hanger and the bottom plate are checked. They are 1/4 ″-20 screws.

6.4.1.1 Tensile Strength

The tensile force on the screws that connect the hinge and the suspend hanger is $F_s / 2$, while the tensile force on the screws that connect the suspend hanger and the bottom plate is $F_b / 4$. According to Eqn. (6.5) and (6.7),

$$\begin{aligned} F_{s\max} / 2 &= 47.007\,\text{N} \\ F_{b\max} / 4 &= 22.336\,\text{N} \end{aligned} \tag{6.11}$$

Therefore, the screws that connect the hinge and the suspend hanger were checked first,

$$\sigma = \frac{F_{s\max} / 2}{A} = \frac{F_{s\max} / 2}{\pi d^2 / 4} = 1.484\,\text{MPa} < [\sigma] = 1100\,\text{MPa} \tag{6.12}$$

6.4.1.2 Shear Strength

The shear force on the screws that connect the hinge and the suspend hanger is $f / 2$, while the shear force on the screws that connect the suspend hanger and the bottom plate is $f_b / 4$ and $f_s / 4$ for the portions of the screws in the holes of the suspend hanger and the bottom plate respectively. According to Eqn. (6.6), (6.8) and (6.9),

$$\begin{aligned} f_{\max} / 2 &= 47.007\,\text{N} \\ f_{s\max} / 4 = f_{b\max} / 4 &= 22.336\,\text{N} \end{aligned} \tag{6.13}$$

Therefore, the screws that connect the hinge and the suspend hanger were checked first,

$$\tau = \frac{f_{\max} / 2}{A} = \frac{f_{\max} / 2}{\pi d^2 / 4} = 1.484\,\text{MPa} < [\tau] = 732\,\text{MPa} \tag{6.14}$$

6.4.2 Strength Check of Suspend Hanger

The material of suspend hanger is Aluminum 6061-T6. Its tensile yield strength and bearing yield strength are 276 MPa and 386 MPa respectively [46].

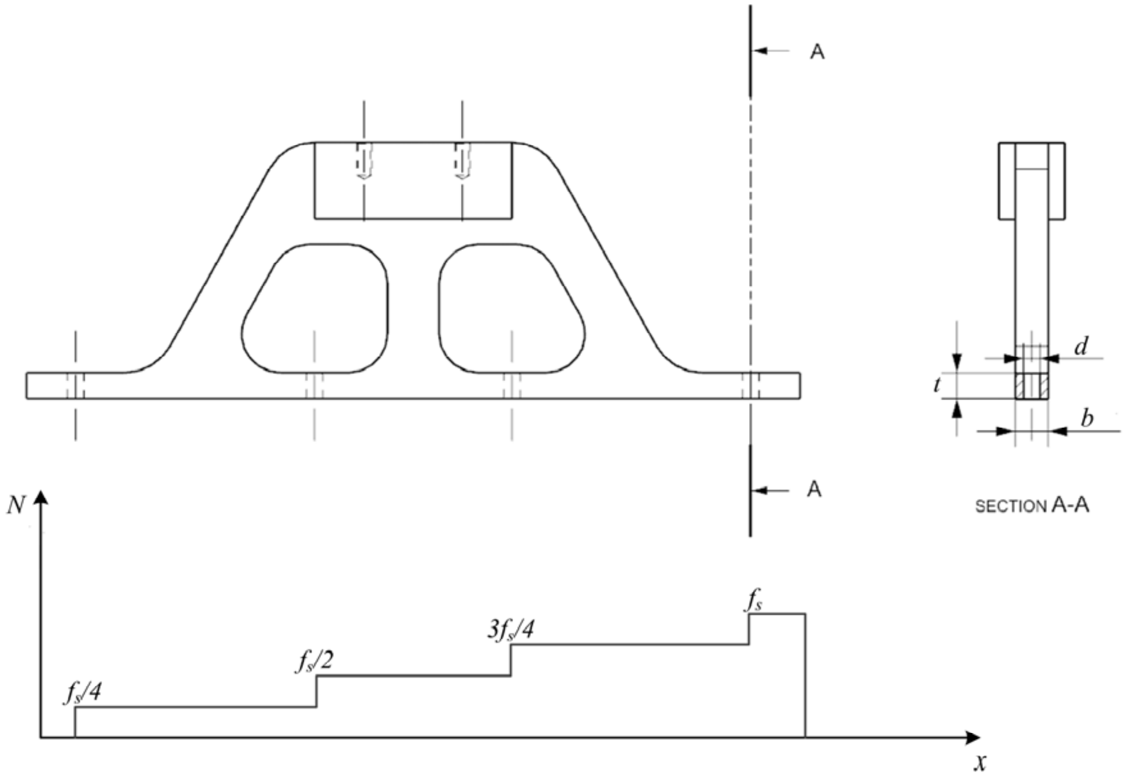

Fig. 6.16: Tensile force on the suspend hanger bottom joints.

6.4.2.1 Tensile Strength

As the cross section area of the suspend hanger bottom is very small, the tensile strength near the joints that connect the suspend hanger and the bottom plate is checked (Fig. 6.16). The tensile force on cross section A-A is the maximum, f_s. When $\theta = 90°$, the stress can be expressed as:

$$\sigma = \frac{f_{s\max}}{A} = \frac{f_{s\max}}{(b-d)t} = 1.407\,\text{MPa} < [\sigma] = 276\,\text{MPa} \tag{6.15}$$

6.4.2.2 Bearing Strength

The bearing force on each of the 4 bottom joints of the suspend hanger is $f_s/4$. Therefore, when $\theta = 90°$, the stress can be expressed as:

$$\sigma = \frac{f_{s\max}/4}{A} = \frac{f_{s\max}/4}{dt} = 0.352\,\text{MPa} < [\sigma] = 386\,\text{MPa} \tag{6.16}$$

6.4.3 Strength Check of Bottom Plate

As the cross section area of the bottom plate is large, only the bearing strength of the joints was checked. The material of the bottom plate is the same as that of the suspend hanger.

6.4.3.1 Bearing Strength

The bearing force on each of the joint is $f_b/4$. Therefore, when $\theta = 90°$, the stress can be expressed as:

$$\sigma = \frac{f_{b\max}/4}{A} = \frac{f_{b\max}/4}{dt} = 0.277\,\text{MPa} < [\sigma] = 386\,\text{MPa} \tag{6.17}$$

6.4.4 Torque on Hinge Check

The gravities of rotary table components exert torque on the hinges when the table is rotated to an angle. The distances between the gravity centers of the components and the rotation axis of the hinge are illustrated in Fig. 6.17. The distances can be expressed as:

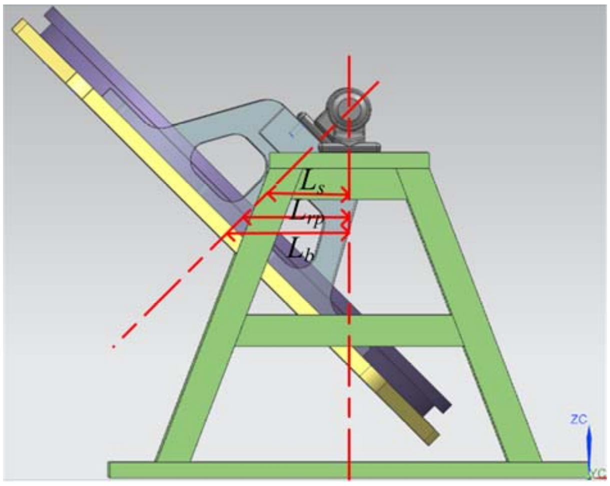

Fig. 6.17: Distance between gravity centers of components to rotation axis.

$$\begin{cases} L_s = (35+100/2)\sin\theta = 85\sin\theta \\ L_{rp} = (35+100-24/2)\sin\theta = 123\sin\theta \\ L_b = (35+100+12.7/2)\sin\theta = 141.35\sin\theta \\ L_p = (35+100-24)\sin\theta = 111\sin\theta \end{cases} \tag{6.18}$$

where L_p is the distance from the gravity center of the measured part to the rotation axis.

Therefore, the torque on the hinges is,

$$T = 2G_s L_s + G_{rp} L_{rp} + G_b L_b + G_p L_p = 22749.241\sin\theta \tag{6.19}$$

When $\theta = 90°$, $T_{\max} = 22749.241\ \mathrm{N\cdot mm}$. The allowable torque of the hinge is 500 in-lbs = 56490 N·mm > $T_{\max}$.

Chapter 7

Multiple-Orientation Scanning

In this section, the workpiece was scanned from different orientations using the blue LED scanner with the facility of the rotary table. Point clouds from different orientations were transformed into a common coordinate system and merged together. Then the merged point cloud was aligned and compared with the CAD model using software Geomagic Qualify 12 [42]. To verify the accuracy of the scanner data, the workpiece was measured using analog touch probe. The probe data was aligned with the CAD model, and compared with the CAD model and the scanner data respectively.

7.1 Point Cloud Acquisition and Merging

As discussed in Section 2.5, to obtain all the top surfaces with various normal directions, the workpiece was fixed on the lightweight rotary table, and scanned by the blue LED scanner at different orientations. The tooling spheres were touch probed at each orientation for coordinate system registration that transforms point clouds from different orientations into a common coordinate system. Here, the point clouds were all transformed to the horizontal point set in CMM MCS. The sphere centers in CMM MCS were determined using Orthogonal Least Squares of GEOMeasure [41]. The registration HTM for the ith orientation, $HTM_{Ori \to Hor,i}$, was obtained by least-square fitting the ith oriented point set and the horizontal point set of the sphere centers [47]. The scanner data from different view angles were first transformed to the CMM MCS with $HTM_{LCS \to MCS}$ (Eqn. (5.5)). At each orientation, several snapshots were taken to scan the whole workpiece. Point clouds of snapshots at the same orientation were merged together, and thinned to be an evenly spaced set of points using software Geomagic Qualify to avoid overlapped areas. The non-horizontal point clouds were then transformed to the horizontal point set (Eqn. (7.1)), merged together, and thinned again.

$$P_{MCS}^{Hor} = HTM_{Ori \to Hor,i} \cdot P_{MCS}^{Ori} \tag{7.1}$$

7.1.1 Scanner Parameters

In multiple-orientation scanning, the scanner was set to work in independent triangulation mode as described in Section 2.1.2 so that occlusion due to extruding features of the workpiece can be reduced. The resolution was set to be the highest 0.1 mm, and the active area was set as default (full). The exposure was set using the “Auto Set” function. As the normal directions of the surfaces were different, the light reflection was different. Multiple exposures were thus used to increase the ability to detect light and dark materials that are in the field of view simultaneously [16]. The frame rate was set as

0.1 Hz to avoid CPU being overloaded, as the highest resolution and multiple exposures were used, and the active area was full.

7.1.2 Noise Reduction and Post Processing

As discussed in reference [48], speckle noise in CCD laser images, caused by wave cancellation or reinforcement, is one of the main sources of random errors in scanner data. Spike noise caused by the weak detection of the laser reflection intensity from inclined surfaces, edges, etc. is another source of random error [49]. Imaging noise can increase uncertainties in measurement result. Therefore, in this thesis work, noise was compensated for using the feature "Reduce Noise" in Geomagic Qualify before post processing the points. This feature moves points to statistically correct locations, leading to a more smooth arrangement of points. To avoid spike noise, point clouds from each orientation were post processed before being merged together. Surfaces with normal vectors close to the vertical direction were kept, while the rest were deleted.

7.2 Alignment and 3D Comparison with CAD Model

The final merged point cloud was aligned with CAD model for 3D comparison. This alignment process is also called data localization in some literature [50]. This is a process of calculating rigid body transformation matrix that transforms the scanner data so that a squared error cost function between the scanner data and the CAD model is minimized. In this thesis, the alignment was performed using the "Best Fit Alignment" feature in Geomagic Qualify that is based on Iterative Closest Point (ICP) algorithm [51]. It works as follows [52]:

1. The scanner data is transformed to a roughly aligned position with the CAD model using an initial guess of the rotation and translation.
2. For each sampled point in the scanner data, P_s, the closest point in the CAD model, P_m, is computed.
3. Utilizing Least Squares method [48], an optimum combination of rotation (R) and translation (T) was found such that the sum of squares of distances between the sample pairs, P_s and P_m, is minimized (Eqn. (7.2)).

$$\begin{aligned} &P_s' = RP_s + T \\ &\text{Minimize}(S = \sum_{i=1}^{n} \left\| \vec{P}_{s,i}' - \vec{P}_{m,i} \right\|^2) \end{aligned} \tag{7.2}$$

4. Iterating Step 2 and 3. Re-compute the closest point in CAD model and establish a new transformation matrix.

After alignment, 3D comparison was performed using software Geomagic Qualify to measure the deviation between the scanner data and the CAD model by generating a three dimensional, color-coded mapping of the deviations. The purpose of 3D comparison was to analyze the accuracy of scanner result.

7.3 Verification with CMM Analog Probe Data

According to the purpose of 3D comparison in Section 7.2, the scanner data should be compared with actual workpiece geometry, given that there may be distortion in actual workpiece. As the analog touch probe is in continuous contact with the workpiece when probing, it has relatively high digitizing speed, and is appropriate for sculptured surface measurement. Moreover, it has lower uncertainty than the scanner (Section 2.1.1.2). Therefore, in this thesis, the workpiece was measured using an analog probe equipped Zeiss Prismo [12]. The obtained probe data was aligned with the CAD model, and compared with the CAD model and the scanner data for accuracy verification. The probe measurement path is illustrated in Fig. 7.1. Five holes of the sheet metal (900 points inside each hole on average), 928 points on flat plane A, and 39 points on sculptured surface B were touch probed.

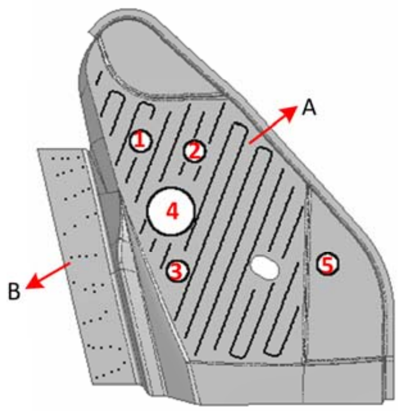

Fig. 7.1: Analog probe measurement path.

7.3.1 Alignment with CAD Model and 3D Comparison

"Feature-Based Alignment" in Geomagic Qualify was used to align the probe data with CAD model. It aligns two objects by pairing corresponding features. In this case, measured points of plane A, hole 2 and 4 were fit into a plane and circles respectively, and paired with the corresponding features of the CAD model. The axes of the holes were used when pairing them.

After the alignment, the probe data was compared with the CAD model and the scanner data respectively using 3D Comparison in Geomagic Qualify. The probe data of the holes were the points inside the hole and below the top surface, while the scanner data of the holes were the points on the top surface. Therefore, only the points on Plane A and B were compared. Before comparison with the scanner data, the point cloud of the scanner data was converted into a polygon object that is consisted of triangle meshes, and spikes were removed. The reason why the probe data was not aligned with the scanner data directly is that, as discussed in Section 7.2, when Best Fit Alignment aligns a point cloud with a polygon object, it minimizes the distance objective function between the two objects. As there are measurement uncertainties in both the scanner data and the probe data, they should be aligned with a common reference set, namely the CAD model, and then compared with each other.

Chapter 8

Experimental Results

Measurement results are presented and analyzed in this chapter. A stamped automotive sheet metal part was measured with the multi-sensor synergistic inspection approach when the rotary table was horizontal as shown in Section 8.1. Next, the sheet metal was measured from multiple orientations with the blue LED scanner by rotating the table as presented in Section 8.2. Finally, the sheet metal was measured with analog probe equipped Zeiss CMM, and the result was compared with the CAD model and scanner data as shown in Section 8.3. Measurement uncertainty of the multi-sensor system is analyzed in Section 8.4.

8.1 Measurement of Horizontal Sheet Metal Part

The five holes of the sheet metal automotive part (Fig. 5.2) were measured with the multi-sensor approach when the table was horizontal (Fig. 3.1(a)). The hole positions and sizes obtained from the CAD nominal geometry, the blue LED scanner, and the touch probe are presented in Tab. 8.1. Starting with the scanner results, the tactile measurements were iterated four times, and finally converged. For brevity, only the initial and the converged tactile measurement results are shown here. The numbers of the holes are illustrated in Fig. 7.1. From the table, it is observed that the actual positions of the holes (the converged results) deviate as much as 0.5 mm from the CAD nominal geometry, but only up to 0.1 mm from the scanner data. Tab. 8.1 also indicates that even the initial tactile measurements are within 4 μm of the converged results, which implies that for typical sheet metal tolerances, much time can be saved by reducing or eliminating iterations. This experiment was performed twice to test the repeatability, and the other measurement result is shown in Tab. 8.2. Tab. 8.2 shows that the initial tactile measurements are within 5 μm of the converged results, which implies high repeatability of the multi-sensor approach.

Hole	CAD Nominal			Blue LED			Touch Probe		
	X	Y	R	X	Y	R	X	Y	R
1	112.012	-57.300	5.000	111.839	-56.805	5.125	111.881 111.882	-56.845 -56.842	4.957 4.957
2	101.342	-80.086	5.000	101.105	-79.688	5.126	101.131 101.133	-79.787 -79.785	4.959 4.960
3	49.128	-58.540	5.000	49.024	-58.161	5.128	48.959 48.959	-58.268 -58.268	4.949 4.950
4	76.738	-62.618	11.000	76.493	-62.195	11.202	76.547 76.547	-62.277 -62.273	10.963 10.963
5	34.714	-126.508	5.000	34.739	-126.112	5.130	34.792 34.793	-126.148 -126.148	4.971 4.971

Tab. 8.1: Measurement results of horizontal sheet metal automotive part (mm).

Only the X and Y positions of the holes were iterated in the experiment, as the heights of the planned touch probe hole points (90° apart along X and Y directions of CMM MCS) were always determined by the scanner data as described in Section 5.2.3. To verify that the scanner results provided effective guidance on the height of the hole points, the center of each adjacent square zone was touch probed. The measurement results are shown in Tab. 8.3. The numbers of the square zones are illustrated in Fig. 5.3. The Z values in Tab. 8.3 are the average height of the points in each adjacent square zone obtained by the blue LED scanner, and the height of the zone center point measured by the touch probe. As can be seen in Tab. 8.3, the maximum deviation between them is 0.074 mm, which is much less than the nominal 1 mm part thickness.

Hole	CAD Nominal			Blue LED			Touch Probe		
	X	Y	R	X	Y	R	X	Y	R
1	112.012	-57.300	5.000	111.846	-56.805	5.128	111.884 111.883	-56.842 -56.837	4.954 4.952
2	101.342	-80.086	5.000	101.136	-79.679	5.124	101.132 101.132	-79.788 -79.787	4.958 4.958
3	49.128	-58.540	5.000	49.042	-58.145	5.129	48.960 48.960	-58.269 -58.267	4.949 4.949
4	76.738	-62.618	11.000	76.508	-62.188	11.201	76.547 76.548	-62.281 -62.276	10.962 10.960
5	34.714	-126.508	5.000	34.780	-126.083	5.132	34.791 34.792	-126.149 -126.148	4.972 4.972

Tab. 8.2: Measurement of horizontal sheet metal automotive part (second test) (mm).

Hole		1				2			
Adjacent Zone		1	2	3	4	1	2	3	4
Z	Blue LED	2.426	2.504	2.426	2.362	2.036	2.125	2.019	1.956
	Probe	2.355	2.443	2.376	2.295	1.974	2.051	1.974	1.908
Hole		3				4			
Adjacent Zone		1	2	3	4	1	2	3	4
Z	Blue LED	2.206	2.220	2.162	2.144	2.291	2.391	2.210	2.084
	Probe	2.147	2.156	2.128	2.094	2.224	2.317	2.161	2.032
Hole		5							
Adjacent Zone		1	2	3	4				
Z	Blue LED	2.042	2.055	2.089	2.021				
	Probe	1.976	2.000	2.049	1.966				

Tab. 8.3: Measurement results of the heights of the adjacent zone points (mm).

8.2 Multiple-Orientation Scanning of the Sheet Metal

The sheet metal was scanned at four orientations (Fig. 3.1(b)), beginning with the horizontal orientation. Using the locking hinges, the table was rotated ~±40°. Finally, the round plate of the rotary table was rotated ~90° with the ring bearing when the table was at ~−40°. The point clouds of different orientations are shown in Fig. 8.1. The tooling spheres were touch probed at each orientation, and the centers were recorded. The sphere centers at each orientation are presented in Tab. 8.4. The corresponding registration transformation matrices were calculated and are also presented here.

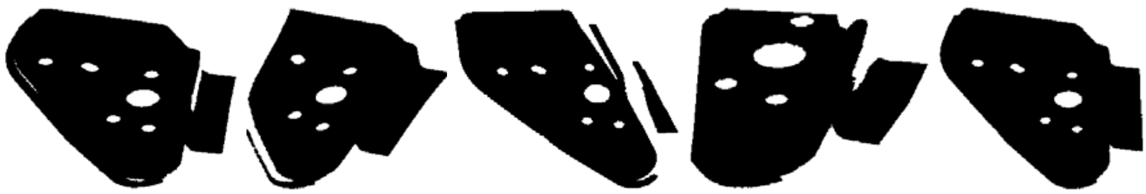

Fig. 8.1: Digitized point clouds of the sheet metal from four orientations: (a) Horizontal, (b) ~+40°, (c) ~−40°, (d) ~90° at ~−40°, (e) Merged cloud of all orientations.

Several snapshots were taken to cover the whole part at each orientation (7 for horizontal orientation, 3 for ~+40°, 4 for ~−40°, and 1 for ~90° at ~−40°). The point clouds of two horizontal snapshots were compared with software Geomagic Qualify 12 (Fig. 8.2). The deviations of points in regions of interest are within 0.033 mm. As shown in Fig. 8.2, the points of large deviation gather on the inclined sculptured surface because its normal direction is non-vertical and spike noise exists in the point clouds.

~+40° Orientation				$HTM_{Ori \rightarrow Hor}$			
Sphere	X	Y	Z	1.0000	-0.0004	0.0014	0.0059
1	-387.313	-169.826	-64.281	-0.0006	0.7777	0.6286	-4.9932
2	-515.225	-323.650	-156.448	-0.0013	-0.6286	0.7777	-177.9735
3	-679.439	-243.959	-92.149	0.0000	0.0000	0.0000	1.0000
~−40° Orientation				$HTM_{Ori \rightarrow Hor}$			
Sphere	X	Y	Z	1.0000	-0.0004	-0.0015	-0.3119
1	-387.352	-219.488	-160.314	-0.0006	0.7693	-0.6389	-111.0834
2	-515.178	-339.873	-27.340	0.0014	0.6389	0.7693	143.4240
3	-679.405	-260.881	-92.481	0.0000	0.0000	0.0000	1.0000
~90° at ~−40° Orientation				$HTM_{Ori \rightarrow Hor}$			
Sphere	X	Y	Z	-0.0049	-0.7694	0.6387	-634.1367
1	-413.986	-356.634	-46.399	1.0000	-0.0057	0.0009	234.7299
2	-590.726	-241.061	-108.910	0.0030	0.6387	0.7695	144.0226
3	-487.460	-115.221	-213.588	0.0000	0.0000	0.0000	1.0000
Horizontal Orientation							
Sphere	X	Y	Z				
1	-387.330	-177.246	-120.684				
2	-515.319	-354.734	-95.487				
3	-679.469	-252.247	-95.360				

Tab. 8.4: Tooling sphere centres and HTM for different orientations (mm).

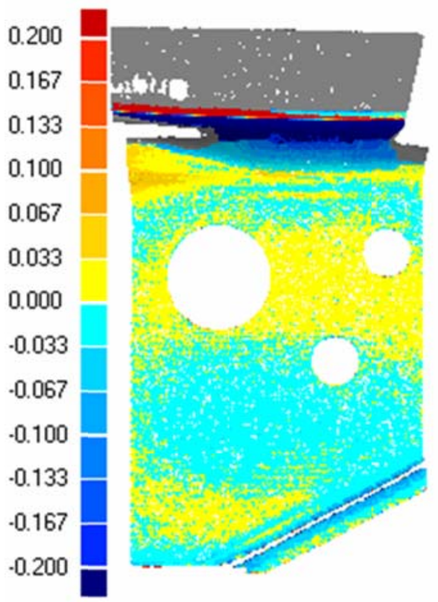

Fig. 8.2: Comparison of horizontal point clouds (mm).

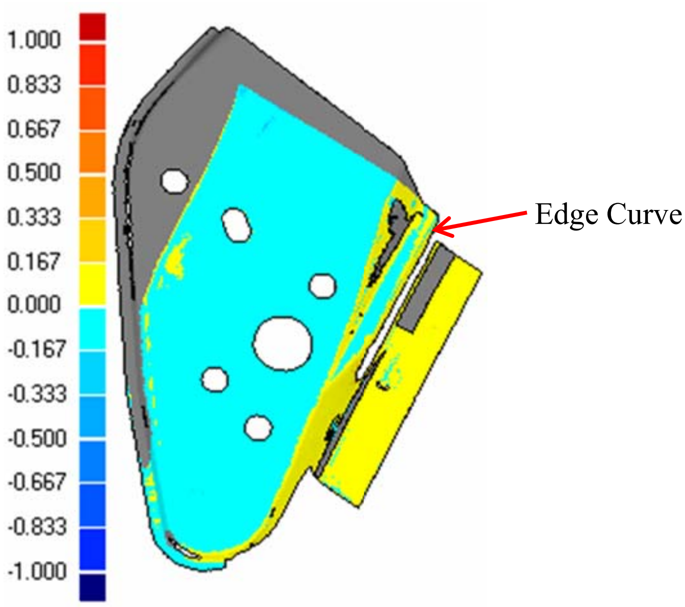

Fig. 8.3: Comparison of horizontal and ~+40° point clouds (mm).

The horizontal point cloud was converted to a polygon object using Geomagic and compared with the ~+40° point cloud (Fig. 8.3). The deviations of points in regions of interest are within 0.167 mm, which is close to the X and Y resolution of the scanner (Tab. 3.1). Large deviation appears on the edge curve of the horizontal polygon surface as shown in Fig. 8.3, because the curve is edge of the horizontal polygon surface, but not for the ~+40° point cloud (Fig. 8.1(a), (b)). Forming of mesh facets on the edge when converting the horizontal point cloud to the polygon object leads to the large deviation. Fig. 8.2 and Fig. 8.3 present high accuracy of $HTM_{LCS \rightarrow MCS}$ and $HTM_{Ori \rightarrow Hor}$ respectively.

Finally, the point clouds of all orientations were post processed to reduce spike noise, merged together, thinned, and compared with the CAD nominal geometry. The post processed point clouds are shown in Fig. 8.4. The deviations of the points are within 0.474 mm (Fig. 8.5), except that larger deviations appear on the edge sculptured surfaces.

The deviations are large possibly due to actual workpiece distortion from the CAD nominal. This was later verified with analog probe data (Section 8.3).

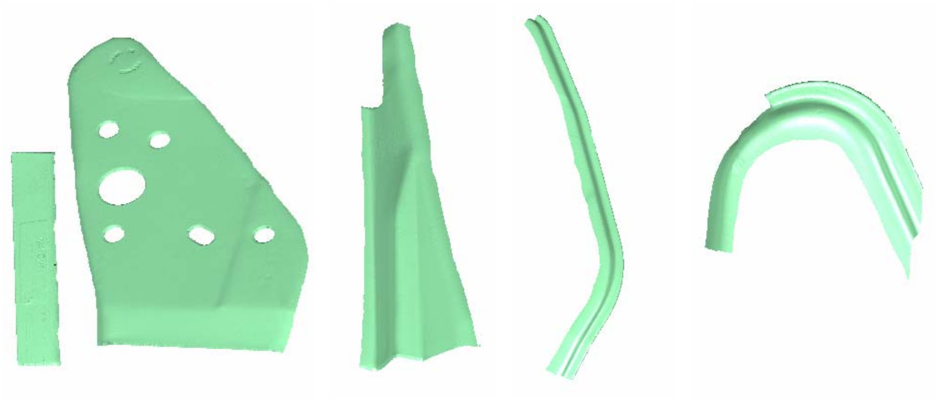

Fig. 8.4: Post processed point clouds of the sheet metal from four orientations: (a) Horizontal, (b) ~+40°, (c) ~−40°, (d) ~90° at ~−40°.

The distances between the tooling spheres at the four orientations were calculated and are presented in Tab. 8.5. The numbers of the spheres are shown in Fig. 3.1(b). The maximum deviation of the distances at non-horizontal orientations from the distances when horizontal is 0.035 mm, which implies that the rotary table has high rigidity.

Orientation		Horizontal	~+40°	~−40°	~90° at ~−40°
Distance between Spheres	1-2	220.267	220.268	220.259	220.232
	2-3	193.517	193.524	193.529	193.539
	1-3	302.674	302.671	302.671	302.706

Tab. 8.5: Distances between tooling spheres at different orientations (mm).

8.3 Measurement of Sheet Metal with Analog Touch Probe

To analyze the accuracy of the scan result, the sheet metal was measured with analog touch probe equipped Zeiss at horizontal orientation. The touch probe data was then aligned with the CAD model as described in Section 7.3.1, and compared with the CAD model and the scan result (Fig. 8.6). As can be seen, there is deviation between the probe data and the CAD nominal, which implies that there is deformation in the actual workpiece. The standard deviation between the probe data and the scanner data is only 0.132 mm, which is much smaller than that in the comparison 3D map between the scanner data and the CAD model (Fig. 8.5), and is also within the X and Y resolution range of the scanner (Tab. 3.1). This verifies high accuracy of the scan result.

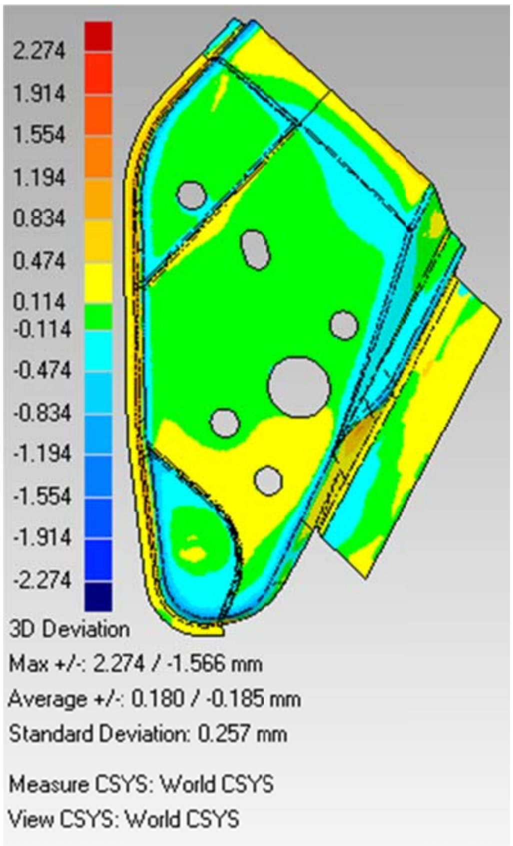

Fig. 8.5: Comparison of merged point cloud and CAD nominal.

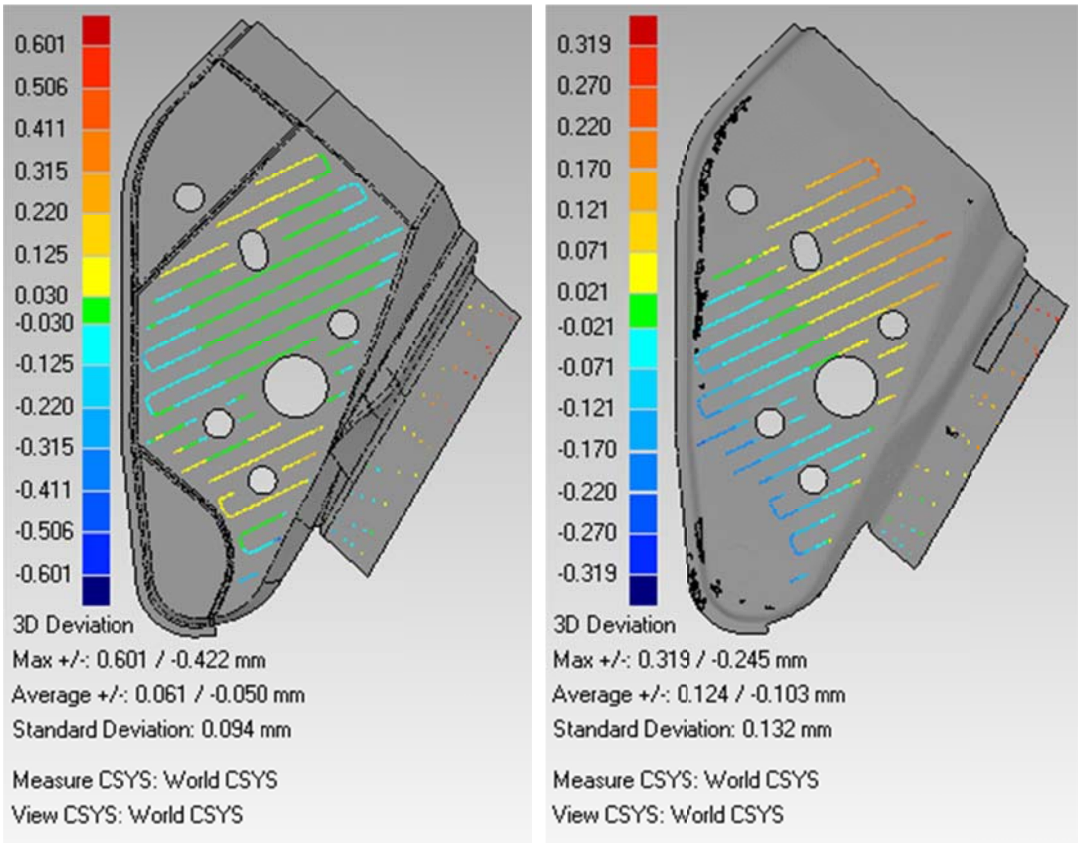

Fig. 8.6: Probe point cloud comparison: (a) Comparison with CAD nominal, (b) Comparison with scanner data.

The analog probe data of the sheet metal holes were imported into Geomagic Qualify and best fit into cylinders. The radii were obtained and compared with the touch-trigger probe results (Tab. 8.6). The maximum deviation between them is only 8μm, which verifies the high accuracy of the touch-trigger probe measurement result.

Hole		1	2	3	4	5
Radius (mm)	Trigger Probe	4.957	4.960	4.950	10.963	4.971
	Analog Probe	4.961	4.952	4.945	10.963	4.968
Number of Points by Analog Probe		898	909	897	909	887

Tab. 8.6: Comparison of hole radius obtained by touch-trigger probe and analog probe.

8.4 Measurement Uncertainty of the System

Expression of measurement uncertainty is an important assessment of confidence in the developed multi-sensor inspection system, and its ability to guide part acceptance/rejection decisions [53]. Contributions to the overall uncertainty arise from performance of hardware components and software, displacement in the fixtures, mathematical algorithms, temperature, and so forth. The major contributors, and their combined uncertainty influence, are:

- DEA IOTA-P CMM Volumetric Uncertainty
- Touch-Trigger Probe System
- Blue LED Scanner System
- Multi-Sensor Extrinsic Calibration
- Fixturing System Displacement
- Temperature

8.4.1 CMM and Touch-Trigger Probe System

As noted in Section 2.6, every orthogonal CMM has 21 volumetric error components [10]. Before using the developed system, a service provider assessed the volumetric errors of the DEA IOTA-P CMM using a laser interferometer and ball bar. All errors, other than linear scale and squareness, were negligible. The linear scales use a stainless steel substrate. Specific Coefficient of Thermal Expansion (CTE) information is not available, and hence a generic value, $\alpha_{\text{scale}} = \left(16 \pm 2\right) \times 10^{-6} /°\text{C}$, was chosen. The laboratory temperature is maintained at $T = 20 \pm 2^{\circ}\text{C}$. The maximum travel lengths for the axes are $\text{X}_{\text{max}} = 750\ \text{mm}$, $\text{Y}_{\text{max}} = 475\ \text{mm}$, $\text{Z}_{\text{max}} = 275\ \text{mm}$. With this information, the method described in [53] can now be used to calculate the linear (or length from origin) uncertainty for each axis. Beginning with the X axis,

$$u_{\alpha,\text{X}}\left(L\right) = \frac{L\Delta T\left(\alpha_{\text{max}} - \alpha\right)}{\sqrt{3}} = \frac{0.750\ \text{m} \times 2^{\circ}\text{C} \times 2 \times 10^{-6}\ /^{\circ}\ \text{C}}{1.732} = 1.7\ \mu\text{m} \tag{8.1}$$

$$u_{T,\text{X}}\left(L\right) = \frac{L\alpha\left(T_{\text{max}} - T\right)}{\sqrt{3}} = \frac{0.750\ \text{m} \times 16 \times 10^{-6}\ /^{\circ}\ \text{C} \times 2^{\circ}\text{C}}{1.732} = 13.9\ \mu\text{m} \tag{8.2}$$

$$u_{\text{X}}^{\text{th}}\left(L\right) = \sqrt{1.7^2 + 13.9^2} = 14.0\ \mu\text{m} \tag{8.3}$$

Similarly, $u_{\alpha,\text{Y}}\left(L\right) = 1.1\ \mu\text{m}$, $u_{T,\text{Y}}\left(L\right) = 8.8\ \mu\text{m}$, $u_{\text{Y}}^{\text{th}}\left(L\right) = \sqrt{1.1^2 + 8.8^2} = 8.9\ \mu\text{m}$, $u_{\alpha,\text{Z}}\left(L\right) = 0.6\ \mu\text{m}$, $u_{T,\text{Z}}\left(L\right) = 5.1\ \mu\text{m}$, and $u_{\text{Z}}^{\text{th}}\left(L\right) = \sqrt{0.6^2 + 5.1^2} = 5.1\ \mu\text{m}$. The Renishaw TP6 touch probe is assigned an uncertainty of 2 μm [37]. Using Eqn. (2.6) with a 404 mm long ball bar, the XY squareness error uncertainty is $u\left(\varphi_{\text{XY}}\right) = \frac{0.004\ \text{mm}}{808\ \text{mm}} = 5.0 \times 10^{-6}\ \text{rad}$, or an insignificant maximum of 2.4 μm along the X axis over a 475 mm Y axis length. Similarly, the uncertainties of YZ and ZX squareness errors are a maximum of 1.4 μm along Y axis and 3.8 μm along Z axis respectively. To summarize, in 3D:

$$u_{\text{3D}}^{\text{th}}\left(L\right) = \sqrt{\left(u_{\text{X}}^{\text{th}}\right)^2 + \left(u_{\text{Y}}^{\text{th}}\right)^2 + \left(u_{\text{Z}}^{\text{th}}\right)^2} = \sqrt{14.0^2 + 8.9^2 + 5.1^2} = 17.4\ \mu\text{m} \tag{8.4}$$

$$u_{\text{3D}}\left(\varphi\right) = \sqrt{u^2\left(\varphi_{\text{XY}}\right) + u^2\left(\varphi_{\text{YZ}}\right) + u^2\left(\varphi_{\text{ZX}}\right)} = \sqrt{2.4^2 + 1.4^2 + 3.8^2} = 4.7\ \mu\text{m} \tag{8.5}$$

8.4.2 Blue LED Scanner System

The resolution of the LMI® Gocator 3110 blue LED scanner utilized in the experiment is higher than 0.15 mm and 0.16 mm in X and Y axis respectively, and 0.108 mm in Z axis. For the X axis, assigning a Type B uniform distribution [53] of width 0.15 mm ($\pm 0.075\,\text{mm}$) yields a standard uncertainty of $\frac{75\,\mu\text{m}}{\sqrt{3}} = 43.3\,\mu\text{m}$. Similarly, the uncertainties for Y and Z axis are $46.2\,\mu\text{m}$ and $31.2\,\mu\text{m}$ respectively. Therefore, $u_{3\text{D}}^{\text{res}} = \sqrt{43.3^2 + 46.2^2 + 31.2^2} = 70.6\,\mu\text{m}$. Although noise in the point clouds obtained from the scanner was reduced using software Geomagic, small amount of noise may still exist in the point cloud as the undesirable image noise varies, and noise reduction is still an interesting research area being investigated by researchers.

8.4.3 Extrinsic Calibration of the Scanner

The input quantities of uncertainty in the extrinsic calibration of the scanner consist of the mathematical algorithm and the flatness of the planes on the calibration target.

8.4.3.1 Calibration Algorithm

The calibration algorithm is made up of the following steps performed on the CMM and the scanner data: plane fitting, plane-plane intersection, line projection and line-line intersection [43]. Plane fitting can have a non-unique solution, depending on the utilized method, and hence needs uncertainty estimation. However, intersection and projection operations have unique solutions, without the need for uncertainty estimation. In the calibration process, the scanner and the CMM data were plane fit in MATLAB [54] and GEOMeasure respectively. The plane fitting results were then utilized to obtain $HTM_{LCS \to MCS}$.

To analyze the uncertainty in the implemented algorithm for plane fitting of the scanner data, testing was performed on 30 reference planar data sets provided by NIST ATS [10],[55],[56]. The reference data was fit to planes utilizing the implemented algorithm in MATLAB. The obtained plane centers and normal directions were compared with the results from NIST. Root Mean Square (RMS) of the differences between the results is reported as the uncertainty [10],[53]. The uncertainty in plane center is 2.9×10^{-13} mm or 2.9×10^{-10} μm, and the uncertainty in plane normal is 7.2×10^{-9} rad. The center position uncertainty is close to the floating point precision of MATLAB (10^{-15} mm, the reference data is in mm). The uncertainty in normal is close to the angle calculation precision of MATLAB, estimated based on its floating point precision, as $\arccos(1-10^{-15}) = 4.5\times10^{-8}$ rad. Plane fitting results of the scanner data were output to 6 decimal places (10^{-6} mm, or 10^{-3} μm). Therefore, the uncertainty in the implemented plane fitting algorithm is,

$$u_{pf} = \sqrt{\left(10^{-3}\right)^2 + \left(10^{-3}\right)^2} = 1.4\times10^{-3}\ \mu\text{m} \tag{8.6}$$

Plane fitting of the CMM data was performed in GEOMeasure. Since widely utilized software like GEOMeaure are assumed to be standardized by NIST ATS, the accuracy of the GEOMeasure plane fitting algorithm is expected to be the same as the

NIST algorithm [57], up to the floating point precision. Therefore, the uncertainty of the GEOMeasure plane fitting algorithm, u_{GEO}, is the set floating point precision of the software output, which in this case is 10^{-6} mm, or $10^{-3}\,\mu\mathrm{m}$.

8.4.3.2 Flatness of Target Planes

The angled slot calibration target consists of five planar features, one top plane and four inclined planes of the slots. The flatness of the planar features can lead to uncertainty in the estimation of the position of their centers and direction of their normals, thus affecting the calibration HTM. During calibration, 30 points on the top plane and 20 points on each inclined plane were touch probed. The CMM data of each plane was imported into Geomagic, fit into a plane, and the flatness was obtained. Four sets of the CMM data were analyzed, and the average of the flatness values was recorded as the flatness of each plane. The data is presented in Tab. 8.7. The flatness values of the planes are utilized to calculate the uncertainty caused by flatness:

$$u_f = \sqrt{15.8^2 + 10.3^2 + 10.5^2 + 3.4^2 + 20.0^2} = 29.6\,\mu\mathrm{m} \tag{8.7}$$

This estimation may result in a higher uncertainty than actual observation, as the flatness of each plane is utilized as the input quantity. Nonetheless, this is commonly seen in practice.

To summarize, the uncertainty in the calibration process is,

$$u_{cal} = \sqrt{u_{pf}^2 + u_{\mathrm{GEO}}^2 + u_f^2} = \sqrt{\left(1.4\times10^{-3}\right)^2 + \left(10^{-3}\right)^2 + 29.6^2} = 29.6\,\mu\mathrm{m} \tag{8.8}$$

Plane \ Data Set	1	2	3	4	Average
+X	16.0	14.0	18.2	14.8	15.8
−X	9.6	11.6	11.1	9.0	10.3
+Y	8.6	9.4	10.6	13.6	10.5
−Y	3.8	3.3	3.5	3.2	3.4
Top	24.2	18.5	19.1	18.2	20.0

Tab. 8.7: Flatness of the five planes on the calibration target (μm).

8.4.4 Fixturing System Displacement

Although strength of the rotary table was checked during design, small displacement in the table is unavoidable. Displacements usually occur during measurement when rotating the table, which can be seen from Tab. 8.5. This affects the accuracy of coordinate system registration using the tooling sphere centers. To evaluate the standard uncertainty caused by the displacement of the rotary table, Type A evaluation was utilized [53]. The data in Tab. 8.5 was analyzed. The standard deviation of the measured distances between spheres 1-2 at different orientations was calculated using Eqn. (A-2) in [53], and the value is $s_{1-2} = 16.8\,\mu\text{m}$. Similarly, the standard deviations of the distances between spheres 2-3 and 1-3 are $s_{2-3} = 9.3\,\mu\text{m}$, $s_{1-3} = 17.1\,\mu\text{m}$. The standard deviations were then combined, weighted by the number of measurements in each data set using Eqn. (A-3) in [53]:

$$s = \sqrt{\frac{3\times s_{1-2}^2 + 3\times s_{2-3}^2 + 3\times s_{1-3}^2}{4+4+4-3}} = 14.8\,\mu\text{m} \qquad (8.9)$$

Therefore, the standard uncertainty caused by the rotary table displacement is $u_{rt} = 14.8\,\mu\text{m}$. This includes the uncertainty of the GEOMeasure sphere fitting algorithm.

8.4.5 Summary

Assuming all the input quantities of uncertainty are uncorrelated, the method of Root Sum of Squares (RSS) is employed to calculate the combined uncertainty [53] of the multi-sensor system:

$$\begin{aligned} u_c &= \sqrt{\left(u_{3\mathrm{D}}^{\mathrm{th}}\left(L\right)\right)^2 + u_{3\mathrm{D}}^2\left(\varphi\right) + \left(u_{3\mathrm{D}}^{\mathrm{res}}\right)^2 + u_{cal}^2 + u_{rt}^2} \\ &= \sqrt{17.4^2 + 4.7^2 + 70.6^2 + 29.6^2 + 14.8^2} \\ &= 80.0\,\mu\mathrm{m} \end{aligned} \tag{8.10}$$

As can be seen, the main influence on the uncertainty is the resolution of the scanner. The expanded uncertainty with a coverage factor of 2 [53], namely an approximate 95% level of confidence of including the true value of the measurand in the uncertainty interval of width $2U$ centered about the measured value (Fig. 8.7), is $U_{k=2} = 2u_c = 160.0\,\mu\mathrm{m}$.

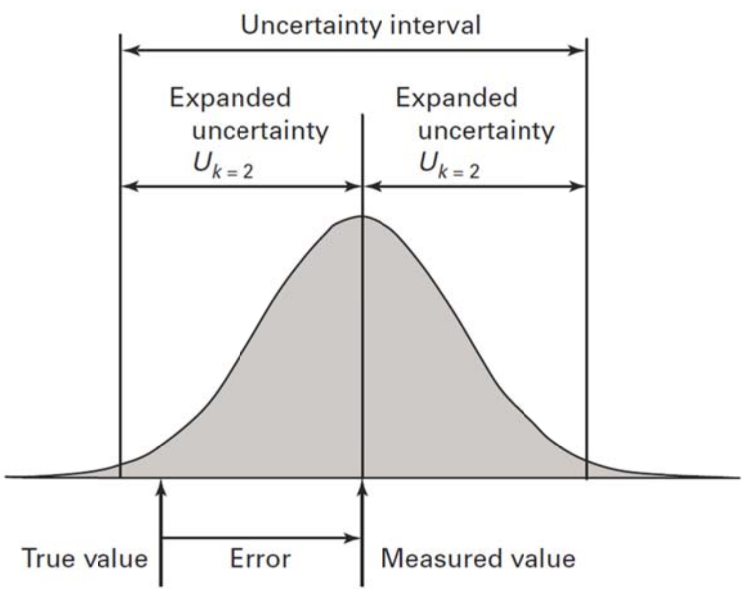

Fig. 8.7: Expanded uncertainty [53].

Chapter 9

Conclusion and Future Works

9.1 Conclusion

The developed multi-sensor inspection system takes advantage of the best characteristics of the touch-trigger probe and the blue LED structured light scanner. After extrinsic calibration of the scanner with respect to the CMM using the angled slot calibration target, the blue LED sensor scanned the part, obtained the approximate sizes and positions of the actual holes and other features. The nominal tactile measurement DMIS program was then adjusted with the scanner data. Finally, successful tactile measurements of features that deviate from nominal geometry and holes on thin sheet metal part were accomplished. As a result, probe missing touches or crashes are avoided. Moreover, much measurement time can be saved with the guidance of the blue LED sensor as iterations of tactile measurement can be reduced or eliminated.

Mechanically aligning the scanner and the CMM axes minimized the angular misalignment between their axes, so that only small remaining angular misalignment needs to be corrected mathematically.

The designed lightweight 2-axis rotary table facilities multiple-orientation scanning for part surfaces or features with normal directions far from vertical direction. Using tooling sphere registration, the point clouds digitized from different orientations can be merged into a common coordinate system.

The horizontal measurement experiment of the stamped sheet metal automotive part verifies the high efficiency and effectiveness of the multi-sensor synergistic inspection. The multiple-orientation scanning experiment confirms the high accuracy of extrinsic calibration of the scanner ($HTM_{LCS \to MCS}$), and the tooling sphere coordinate system registration ($HTM_{Ori \to Hor}$). The analog probe measurement data verifies the high accuracy of the multiple-orientation scanning results.

9.2 Future Works

The developed multi-sensor system in this thesis work was implemented on an orthogonal CMM. In future work, it can be migrated to a portable CMM, or even CNC machine, so that in-line inspection can be accomplished.

The developed C software in this thesis for outputting point clouds digitized by the scanner and scanner measurement results is limited to hole measurement. In future work, a more generic program should be developed for measurement of various kinds of features.

The designed 2-axis rotary table has to be rotated or tilted manually. In future work, remote control of the table may be realized by cable or pneumatic release activation [58].

Appendix A

A.1 Touch-Trigger Probe Bracket with Collar

Unless otherwise specified, all dimensions are in millimetres. Material: aluminum.

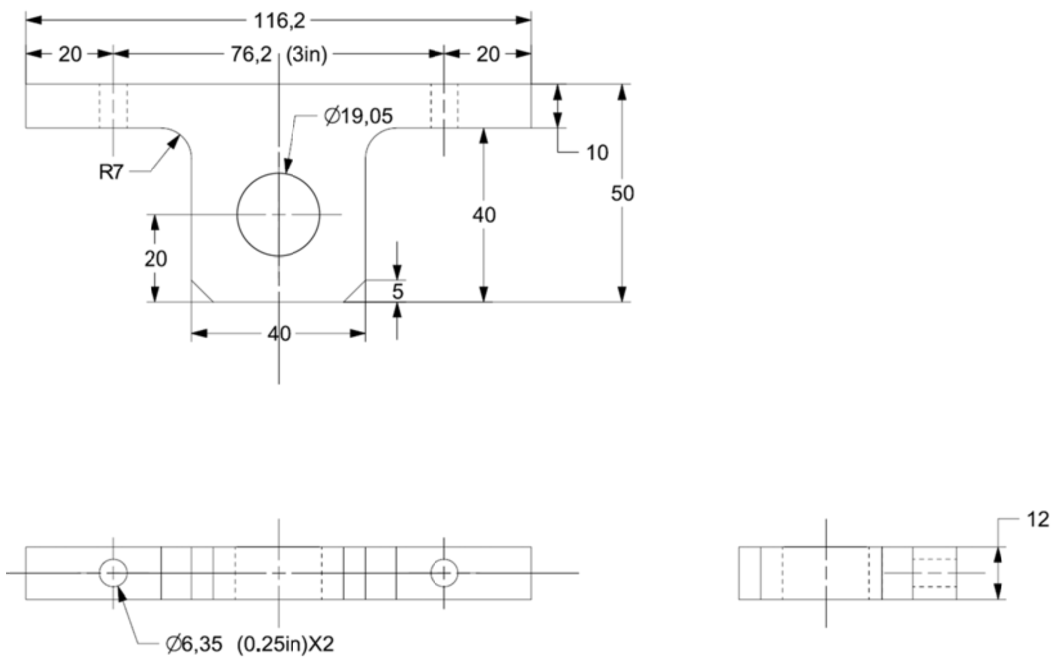

Unless otherwise specified, all dimensions are in inches. Material: stainless steel.

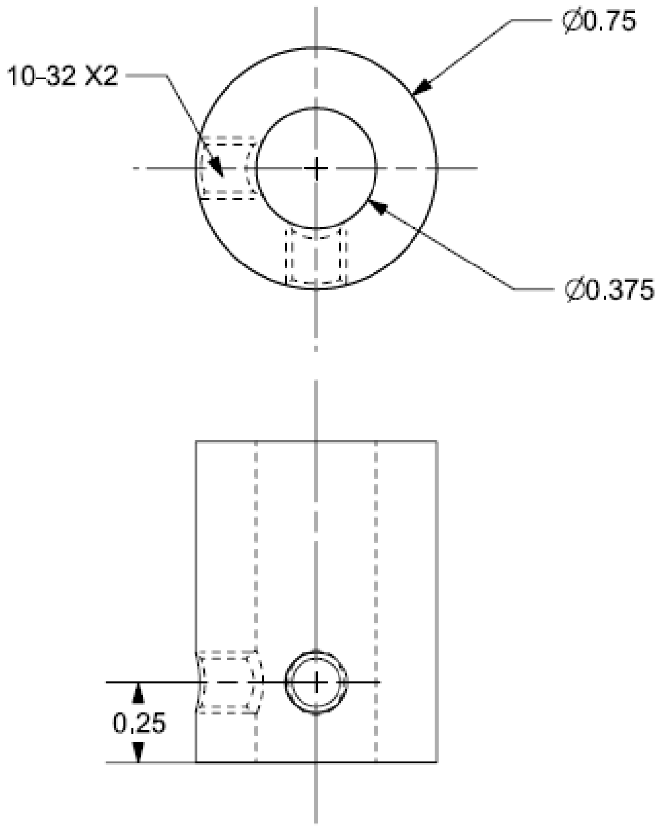

A.2 Scanner Bracket

Unless otherwise specified, all dimensions are in millimetres. Material: aluminum.

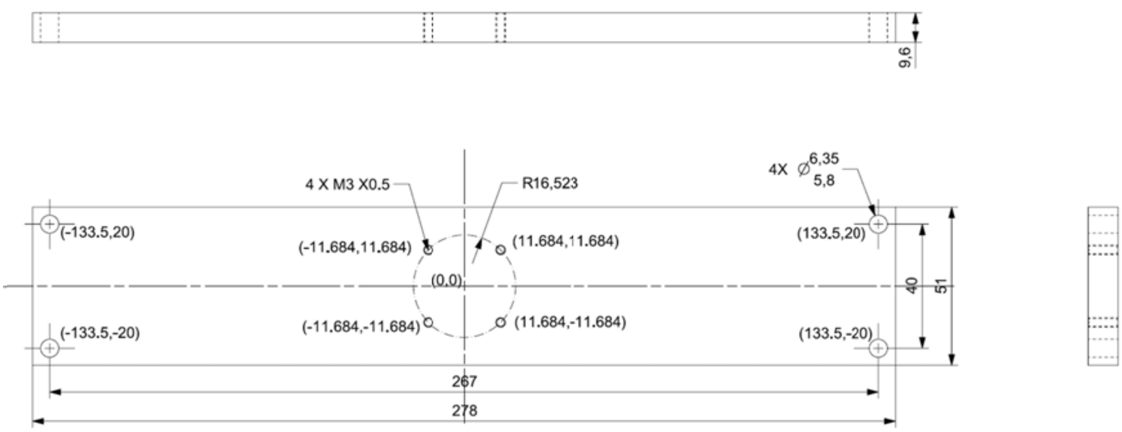

A.3 Renishaw® AM1 Adjustment Module

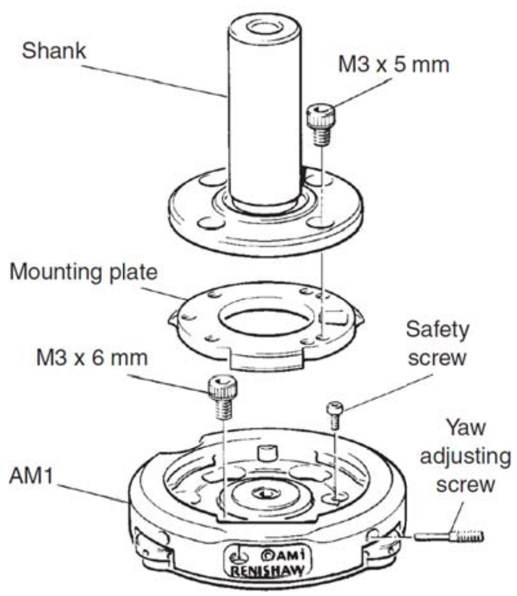

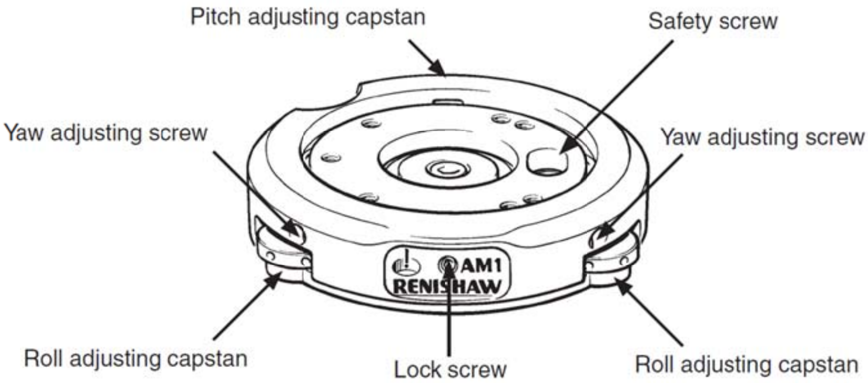
Pitch adjusting capstan
Safety screw
Yaw adjusting screw
Yaw adjusting screw
AM1
RENISHAW
Roll adjusting capstan
Lock screw
Roll adjusting capstan

A.4 Aluminum Collar on CMM Granite Table

Unless otherwise specified, all dimensions are in millimeters. Material: aluminum.

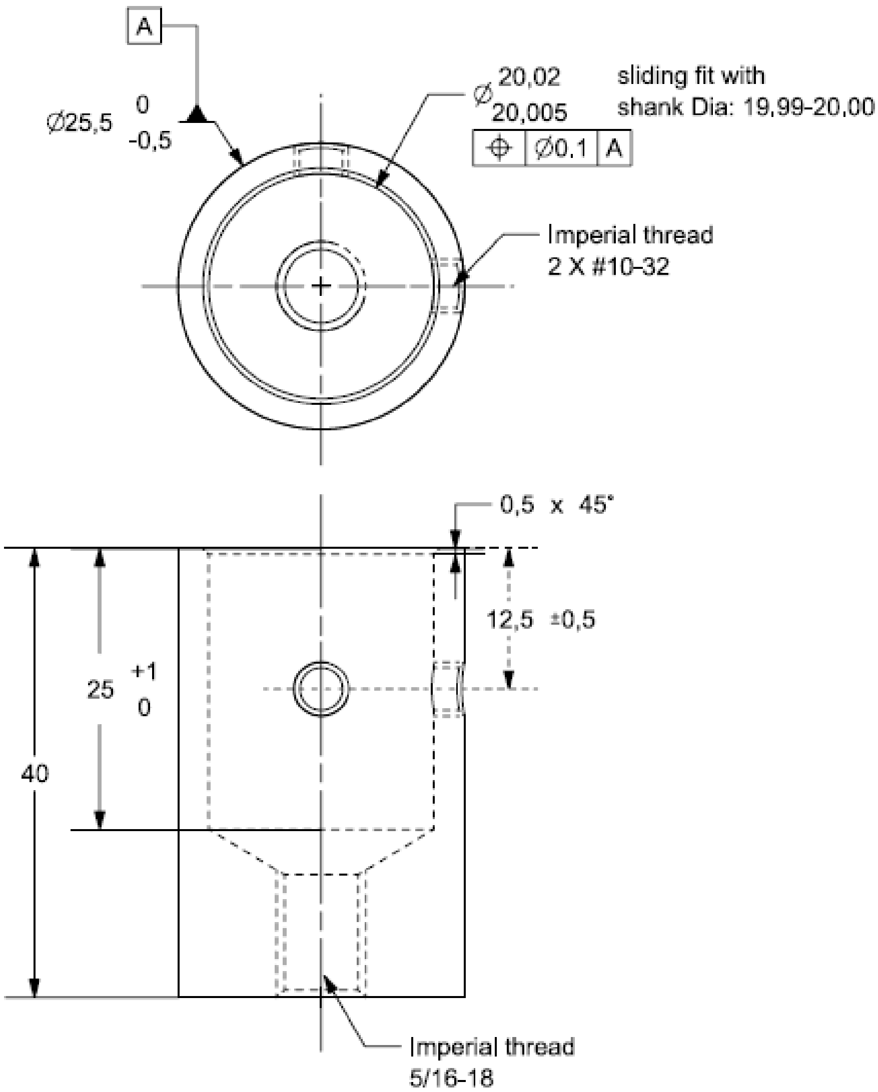

A.5 Bottom Plate

Unless otherwise specified, all dimensions are in millimeters. Material: aluminum.

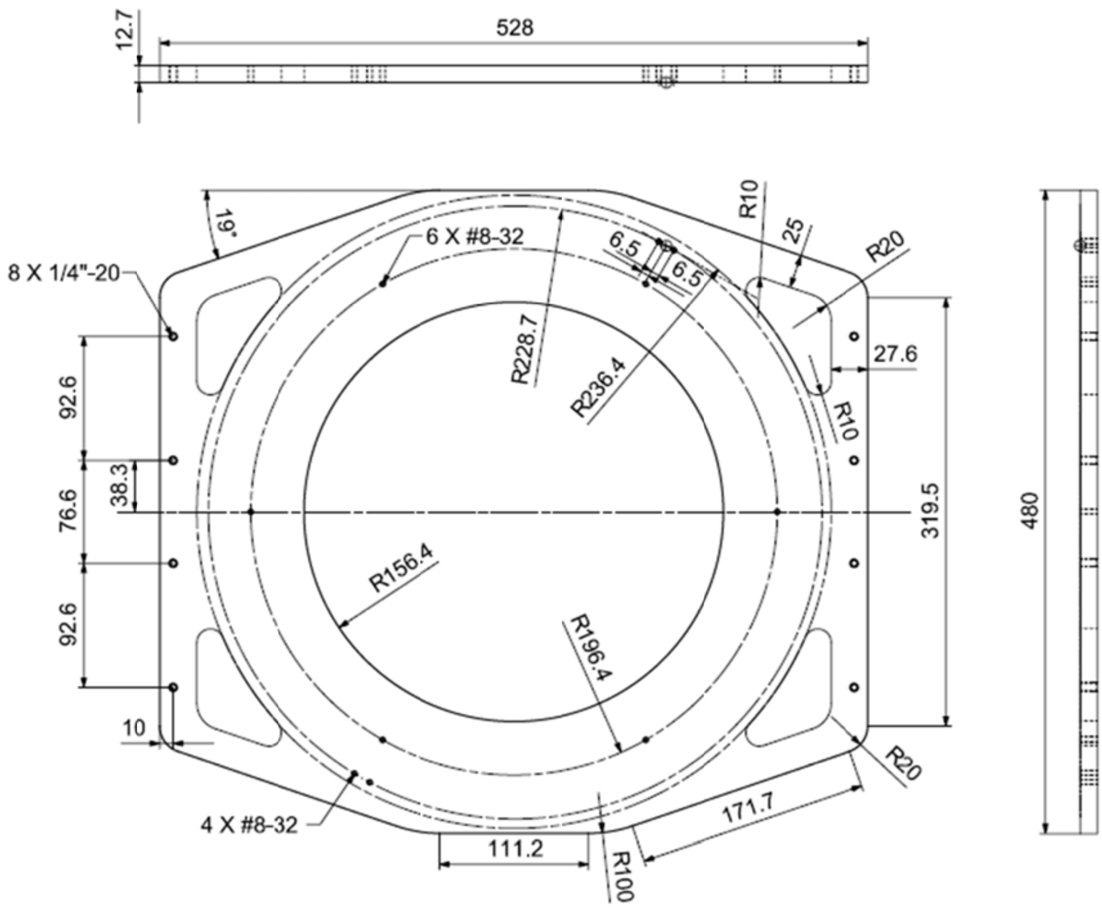

A.6 Vertical Base Support

Unless otherwise specified, all dimensions are in millimeters. Material: aluminum.

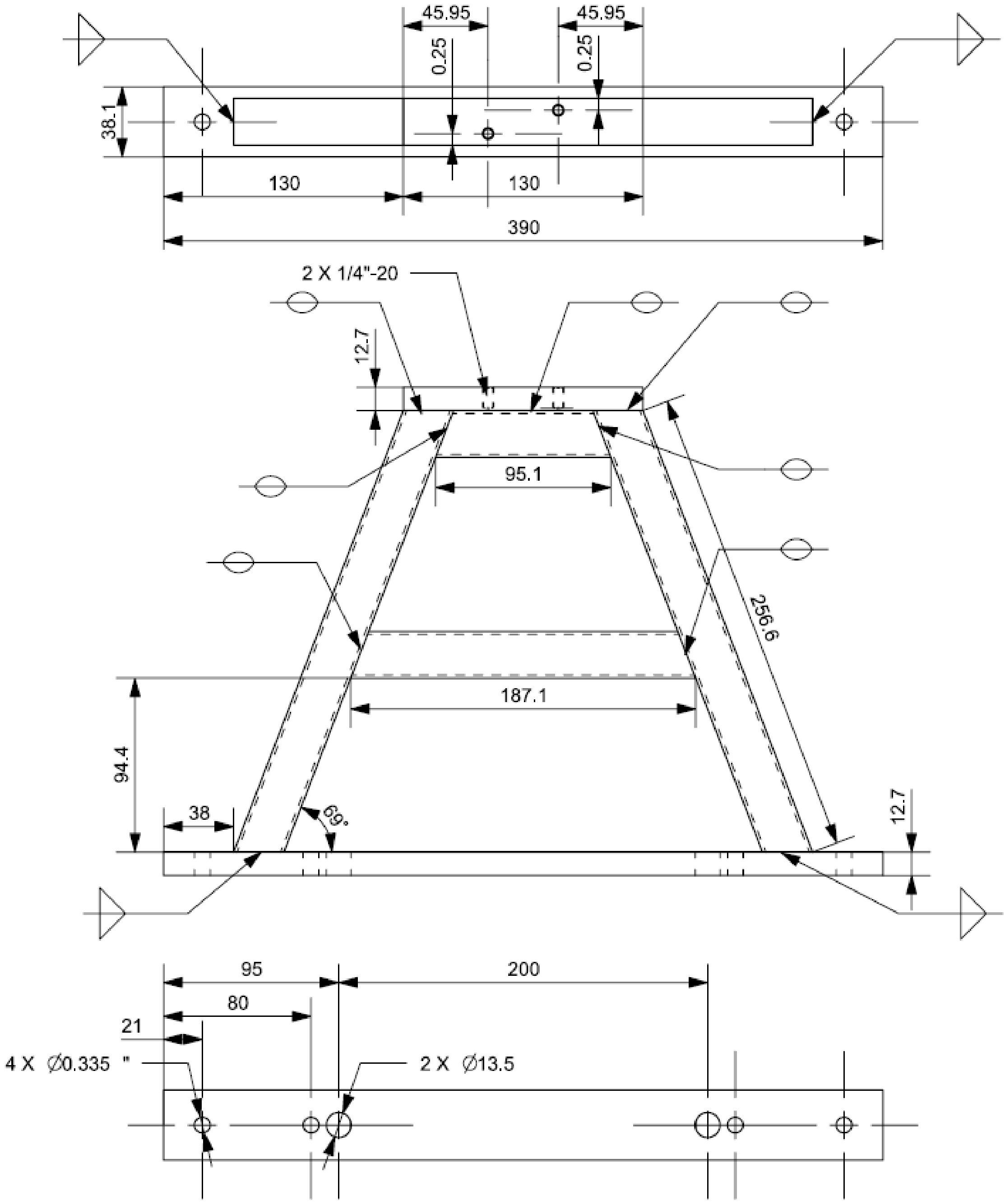

A.7 Suspend Hanger

Unless otherwise specified, all dimensions are in millimeters. Material: aluminum.

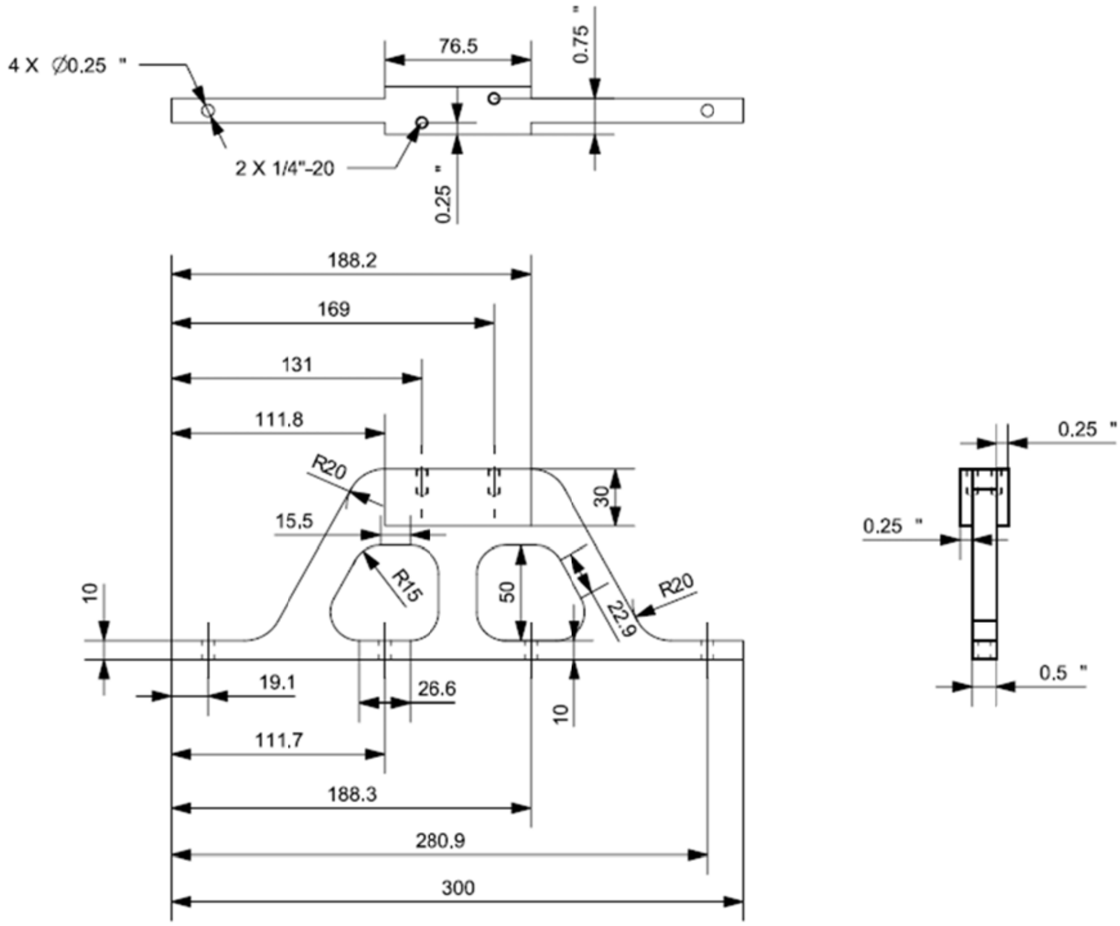

References

[1] A. Weckenmann, P. Kraemer, and J. Hoffmann, "MANUFACTURING METROLOGY – STATE OF THE ART AND PROSPECTS," in *9th INTERNATIONAL SYMPOSIUM ON MEASUREMENT AND QUALITY CONTROL (9th ISMQC)*, 2007.

[2] H. Kunzmann, T. Pfeifer, R. Schmitt, H. Schwenke, and W. A., "Productive Metrology - Adding Value to Manufacture," *CIRP Ann. - Manuf. Technol.*, vol. 54, no. 2, pp. 155–168, 2005.

[3] A. Weckenmann, T. Estler, G. Peggs, and D. McMurtry, "Probing Systems in Dimensional Metrology," *CIRP Ann. - Manuf. Technol.*, vol. 53, pp. 657–684, 2004.

[4] B. R. Barbero and E. S. Ureta, "Comparative study of different digitization techniques and their accuracy," *CAD Comput. Aided Des.*, vol. 43, no. 2, pp. 188–206, 2011.

[5] Joint Committee for Guides in Metrology (JCGM), "Evaluation of measurement data: Guide to the expression of uncertainty in measurement," 2008.

[6] A. P. Karafillis and M. C. Boyce, "Tooling and binder design for sheet metal forming processes compensating springback error," *Int. J. Mach. Tools Manuf.*, vol. 36, no. 4, pp. 503–526, 1996.

[7] F. Kosel, T. Videnic, T. Kosel, and M. Brojan, "Elasto-Plastic springback of beams subjected to repeated bending/unbending histories," *J. Mater. Eng. Perform.*, vol. 20, pp. 846–854, 2011.

[8] A. Weckenmann, P. Gall, and A. Gabbia, "3D surface coordinate inspection of formed sheet material parts using optical measurement systems and virtual distortion compensation," vol. 5776, pp. 640–647, 2005.

[9] M. Halioua, R. S. Krishnamurthy, H. C. Liu, and F. P. Chiang, “Automated 360 degrees profilometry of 3-D diffuse objects.,” *Appl. Opt.*, vol. 24, no. 14, p. 2193, 1985.

[10] R. J. Hocken and P. H. Pereira, *Coordinate Measuring Machines and Systems, Second Edition*. CRC Press, 2011.

[11] Renishaw, “User’s guide: Touch-trigger probe systems,” 2014. [Online]. Available: http://resources.renishaw.com/en/details/users-guide-touch-trigger-probe-systems--63688. [Accessed: 13-Mar-2015].

[12] “Carl Zeiss Industrial Metrology,” *Oberkochen, Germany*, 2015. [Online]. Available: http://www.zeiss.com/industrial-metrology. [Accessed: 12-Feb-2015].

[13] “Introduction to CMM Programming and the Cosine Error - Nel Pretech.” [Online]. Available: http://nelpretech.com/introduction-cmm-programming-cosine-error/. [Accessed: 09-Mar-2015].

[14] A. Weckenmann, X. Jiang, K. D. Sommer, U. Neuschaefer-Rube, J. Seewig, L. Shaw, and T. Estler, “Multisensor data fusion in dimensional metrology,” *CIRP Ann. - Manuf. Technol.*, vol. 58, pp. 701–721, 2009.

[15] F. Chen, G. Brown, and M. Song, “Overview of three-dimensional shape measurement using optical methods,” *Opt. …*, vol. 39, no. 1, pp. 10–22, 2000.

[16] LMI, “Manual_Gocator 3x00 Series.” [Online]. Available: http://www.lmi3d.com/manuals/gocator/gocator-4.1/pdf/15199-4.1.4.12_MANUAL_User_Gocator-3x00-Series.pdf. [Accessed: 17-Mar-2015].

[17] “LMI Technologies Inc.,” *Delta, British Columbia, Canada*, 2013. [Online]. Available: http://www.lmi3d.com/. [Accessed: 12-Feb-2015].

[18] 3D Engineering Solutions, “High Resolution Structured Light Scanning / Blue and White Light Scanning.” [Online]. Available: http://www.3d-engineering.net/white-light-scanning.htm. [Accessed: 26-Mar-2015].

[19] J. Geng, “Structured-light 3D surface imaging: a tutorial,” *Adv. Opt. Photonics*, vol. 3, no. 2, p. 128, Mar. 2011.

[20] P. S. Huang, “Novel method for structured light system calibration,” *Opt. Eng.*, vol. 45, no. 8, p. 083601, 2006.

[21] S. Zhang and S.-T. Yau, "High-resolution, real-time 3D absolute coordinate measurement based on a phase-shifting method," *Opt. Express*, vol. 14, no. 7, pp. 2644–2649, 2006.

[22] S. D. Eppinger, D. E. Whitney, and D. E. Whitney, "Generalized Models of Design Iteration Using Signal Flow Graphs," 1996.

[23] W. Gan and R. H. Wagoner, "Die design method for sheet springback," *Int. J. Mech. Sci.*, vol. 46, no. 7, pp. 1097–1113, 2004.

[24] E. Chalpin, "Plastic deformation and stress-strain curves." [Online]. Available: http://athena.ecs.csus.edu/~e45/PLASTIC DEFORMATION BACKGROUND.pdf. [Accessed: 19-Mar-2015].

[25] M. Nashman, W. Rippey, T. H. Hong, and M. Herman, "An Integrated Vision Touch-Probe System for Dimensional Inspection Tasks," *Natl. Inst. Stand. Technol. - NISTIR 5678*, pp. 1–21, 1995.

[26] C. Bradley and V. Chan, "A Complementary Sensor Approach to Reverse Engineering," *J. Manuf. Sci. Eng.*, vol. 123, no. 1, p. 74, 2001.

[27] J. Sladek, P. M. Blaszczyk, M. Kupiec, and R. Sitnik, "The hybrid contact–optical coordinate measuring system," *Measurement*, vol. 44, pp. 503–510, 2011.

[28] Z. Xie, J. Wang, and Q. Zhang, "Complete 3D measurement in reverse engineering using a multi-probe system," *Int. J. Mach. Tools Manuf.*, vol. 45, pp. 1474–1486, 2005.

[29] V. Carbone, M. Carocci, E. Savio, G. Sansoni, and L. De Chiffre, "Combination of a vision system and a coordinate measuring machine for the reverse engineering of freeform surfaces," *Int. J. Adv. Manuf. Technol.*, vol. 17, pp. 263–271, 2001.

[30] T. S. Shen, H. Jianbing, and C.-H. Menq, "Multiple-sensor integration for rapid and high-precision coordinate metrology," *IEEE/ASME Trans. Mechatronics*, vol. 5, no. 2, pp. 110–121, 2000.

[31] A. Mohib, A. Azab, and H. ElMaraghy, "Feature-based hybrid inspection planning: A mathematical programming approach," *Int. J. Comput. Integr. Manuf.*, vol. 22, pp. 13–29, 2009.

[32] H. Zhao, J. P. Kruth, N. Van Gestel, B. Boeckmans, and P. Bleys, "Automated dimensional inspection planning using the combination of laser scanner and tactile probe," *Meas. J. Int. Meas. Confed.*, vol. 45, no. 5, pp. 1057–1066, 2012.

[33] X. Zexiao, Z. Weitong, Z. Zhiwei, and J. Ming, "A novel approach for the field calibration of line structured-light sensors," *Meas. J. Int. Meas. Confed.*, vol. 43, no. 2, pp. 190–196, 2010.

[34] C. Reich, "Photogrammetric matching of point clouds for 3D-measurement," vol. 3520, pp. 100–110, 1998.

[35] H. Ohara, H. Konno, M. Sasaki, M. Suzuki, and K. Murata, "Automated 360° profilometry of a three-dimensional diffuse object and its reconstruction by use of the shading model.," *Appl. Opt.*, vol. 35, pp. 4476–4480, 1996.

[36] "Renishaw plc - PH6," *New Mills, Wotton-under-Edge, Gloucestershire, UK*, 2015. [Online]. Available: http://www.renishaw.ca/en/ph6-ph6m--7393. [Accessed: 12-Feb-2015].

[37] "Renishaw plc - TP6." [Online]. Available: http://www.renishaw.ca/en/tp6-tp6a--7377. [Accessed: 05-Apr-2015].

[38] "Measurement Computing Corporation," *Norton, MA, USA*, 2010. [Online]. Available: http://www.mccdaq.com/. [Accessed: 12-Feb-2015].

[39] "Renishaw plc - AM1 Adjustment Modules." [Online]. Available: http://www.renishaw.com/en/6678.aspx. [Accessed: 05-Apr-2015].

[40] "Siemens PLM Software," *Plano, TX, USA*, 2013. [Online]. Available: http://www.plm.automation.siemens.com. [Accessed: 12-Feb-2015].

[41] "Mitutoyo America Corporation," *Aurora, Illinois, USA*. [Online]. Available: http://www.mitutoyo.com/. [Accessed: 12-Feb-2015].

[42] "Geomagic 3D software from 3D Systems," *Cary, NC, USA*. [Online]. Available: http://www.geomagic.com. [Accessed: 12-Feb-2015].

[43] K. Xue, V. Kurella, and A. Spence, "Multi-Sensor Blue LED and Touch Probe Inspection System," *Comput. Des. Appl.*, vol. 13, 2016.

[44] "Adjustable Locking Technologies - Variloc Medium Duty Stainless Steel Locking Hinges." [Online]. Available: http://www.adjustablelockingtech.com/products_variloc_stainless_mounting-flange.php. [Accessed: 17-Apr-2015].

[45] "12.9 Bolt Shear Capacity | eHow." [Online]. Available: http://www.ehow.com/info_11415080_129-bolt-shear-capacity.html. [Accessed: 25-Apr-2015].

[46] "ASM Material Data Sheet." [Online]. Available: http://asm.matweb.com/search/SpecificMaterial.asp?bassnum=MA6061t6. [Accessed: 10-May-2015].

[47] K. ARUN, S. HUANG, and D. BLOSTEIN, "Least-Squares Fitting of Two 3-D Point Sets," *IEEE Trans. Pattern Anal. Mach. Intell.*, vol. PAMI-9, no. 5, pp. 698–700, 1987.

[48] Y. P. Lin, "Geometrically Adaptive Milling of Fan Blade Assembly Weld Fillets," McMaster University, 2012.

[49] K. Koshino, H. Zuo, N. Saito, and S. Suzuki, "Improved spike noise removal in the scanning laser microscopic image of diamond abrasive grain using wavelet transforms," *Opt. Commun.*, vol. 239, no. 1–3, pp. 67–78, 2004.

[50] D. F. ElKott, "CAD-based CMM Inspection of Sculptured Surfaces," McMaster University (Canada), 2007.

[51] P. Besl and N. McKay, "A Method for Registration of 3-D Shapes," *IEEE Transactions on Pattern Analysis and Machine Intelligence*, vol. 14, no. 2. pp. 239–256, 1992.

[52] "How does Best Fit Alignment determine how the parts are aligned?" [Online]. Available: http://support1.geomagic.com/link/portal/5605/5668/Article/976/How-does-Best-Fit-Alignment-determine-how-the-parts-are-aligned. [Accessed: 17-May-2015].

[53] ASME B89.7.3.2, "Guidelines for the Evaluation of Dimensional Measurement Uncertainty," 2007.

[54] "MATLAB - The Language of Technical Computing." [Online]. Available: http://www.mathworks.com/products/matlab/. [Accessed: 26-Jul-2015].

[55] T. H. Hopp and M. S. Levenson, "Performance-Measures for Geometric Fitting in the NIST Algorithm Testing and Evaluation Program for Coordinate Measurement Systems," *J. Res. Natl. Inst. Stand. Technol.*, vol. 100, no. 5, pp. 563–574, 1995.

[56] C. Diaz, "Concept for an Algorithm Testing and Evaluation Program at NIST," *Natl. Inst. Stand. Technol.*, 1994.

[57] C. M. Shakarji, “Least-squares fitting algorithms of the NIST algorithm testing system,” *J. Res. Natl. Inst. Stand. Technol.*, vol. 103, no. 6, p. 633, 1998.

[58] “How to Use Variloc® Hinges | Pneumatic, Cable and Push Button Release.” [Online]. Available: http://www.adjustablelockingtech.com/products_variloc_activation_overview.php. [Accessed: 26-Jun-2015].